國 立 交 通 大 學

電子工程學系　　電子研究所碩士班

碩 士 論 文

超薄絕緣鍺金氧半場效電晶體在量子侷限下的

短通道效應模型與分析

Modeling and Investigation of Short-Channel Effects

for Ultra-Thin-Body Germanium-On-Insulator MOSFETs

Considering Quantum Confinement

研 究 生：謝欣原

指導教授：蘇　彬　教授

中 華 民 國 九 十 九 年 八 月

超薄絕緣鍺金氧半場效電晶體在量子侷限下的

短通道效應模型與分析

Modeling and Investigation of Short-Channel Effects

for Ultra-Thin-Body Germanium-On-Insulator MOSFETs

Considering Quantum Confinement

研 究 生：謝欣原　　　　　　　　　Student：Hsin-Yuan Hsieh

指導教授：蘇　彬　　　　　　　　　Advisor：Pin Su

國 立 交 通 大 學

電子工程學系　　電子研究所碩士班

碩 士 論 文

A Thesis

Submitted to Department of Electronics Engineering & Institute of Electronics

College of Electrical and Computer Engineering

National Chiao Tung University

in Partial Fulfillment of the Requirements

for the Degree of Master

in

Electronic Engineering

August 2010

Hsinchu, Taiwan, Republic of China

中 華 民 國 九 十 九 年 八 月

超薄絕緣鍺金氧半場效電晶體在量子侷限下的短通道效應模型與分析

研究生：謝欣原　　　　　　　　　指導教授：蘇 彬

國立交通大學電子工程學系
電子研究所碩士班

摘 要

　　鍺作為通道材料已被提出可以提供更高的載子遷移率。然而，它的高介電常數造成其非常易受到短通道效應的影響。為了改善靜電完整性，有著薄埋層氧化層的超薄絕緣鍺金氧半場效電晶體被視作一個有希望的元件結構以繼續 CMOS 的微縮。在本論文裡，我們理論化地探討在超薄絕緣鍺金氧半場效電晶體中量子侷限效應對臨界電壓衰變的衝擊。為了獲得臨界電壓，我們解析 Schrödinger 方程式且根據一個拋物線形式的通道電位來導出量子侷限模型。這拋物線形式的通道電位是從解 Poisson 方程式得到的通道電位級數解簡化得來，且此級數解有正確的通道長度依靠性。因此，我們的量子侷限模型可以用來檢驗超薄絕緣鍺元件的短通道效應。我們的研究指出對於極限微縮的超薄絕緣鍺元件，臨界電壓衰變可以被量子侷限給壓制。

Modeling and Investigation of Short-Channel Effects for Ultra-Thin-Body Germanium-On-Insulator MOSFETs Considering Quantum Confinement

Student：Hsin-Yuan Hsieh   Advisor：Pin Su

Department of Electronics Engineering
Institute of Electronics
National Chiao Tung University

Abstract

Germanium as a channel material has been proposed to enable mobility scaling. However, its high permittivity makes it very susceptible to short-channel effects (SCEs). To improve the electrostatic integrity, ultra-thin-body (UTB) germanium-on-insulator (GeOI) MOSFET with thin buried oxide has been proposed as a promising device architecture to continue CMOS scaling. In this thesis, we theoretically investigate the impact of quantum-mechanical effects on the threshold-voltage (V_T) roll-off in UTB GeOI MOSFETs. To obtain V_T, we have analytically solved the Schrödinger equation and derived a quantum-confinement model based on a parabolic form of channel potential. This parabolic channel potential is simplified from the series solution of Poisson's equation and has the correct dependence of channel length. Therefore, our quantum-confinement model can be used to examine the SCEs for UTB GeOI devices. Our study indicates that for extremely-scaled UTB GeOI devices, V_T roll-off can be suppressed by quantum confinement.

誌　　謝

　　兩年的碩士生涯即將結束，期間最重要的研究成果，也將會呈現在這本碩士論文裡。回憶這兩年研究時光所碰到的種種問題與困難，箇中滋味真是難以言表，所幸最終完成了既定目標，在這論文即將完成的時刻，心中充滿著感動。

　　在研究上，最要感謝的是我的指導教授蘇彬老師。老師在其研究領域的博學多聞以及對於處理問題的方法，都令我印象深刻且受益頗豐。其中對學生在研究上的耐心建議與指導，更令我感到敬佩。此外，特別感謝吳育昇學長和 Vita 學姊在這個題目上給我的幫助和建議，也感謝小郭、銘隆、昆諺三位學長和昌鴻學弟平日裡的討論與關心。俊賢和劭衡二位學弟雖然相處的時間不長，但能夠在這最後寫論文的時間和你們聊天對於我壓力的紓解幫助不小，謝謝你們！

　　最後要謝謝我的家人給我的支持與體諒，兩年的時間很少陪伴在家人身旁，但父母親的電話關心和與姊姊的 MSN 對話聊天，卻都是我碩士班兩年的動力來源。有他們的鼓勵，才會有我今日的成就。

Contents

V

Figure Captions

Table Captions

Chapter 1

Introduction

1.1 Background

Germanium as a channel material has been proposed [1]-[3] to provide higher mobility for CMOS scaling. However, its higher permittivity makes it very susceptible to short-channel effects (SCEs). To improve the electrostatic integrity, ultra-thin-body (UTB) germanium-on-insulator (GeOI) MOSFET with thin buried oxide (BOX) has been proposed as a promising device architecture and shows better control of SCEs than the bulk counterpart [4]-[5]. As the channel thickness scales down, the quantum-confinement effect may become more significant and its impact on the SCEs of UTB GeOI is not clearly known. In this work, we investigate the problem using theoretical calculations.

Since SCEs are closely related to the subthreshold behaviors of UTB devices and the subthreshold characteristics are deeply influenced by the entire channel potential distribution, an analytical channel potential model is crucial to this study.

An analytical 2-D channel potential model with series form for UTB MOSFETs under subthreshold region has been reported in [6]. Since the series solution of channel potential is too complicated to be used in solving the Schrödinger equation when considering quantum mechanism, we need to simplify the series solution. In this thesis, we present a compact form of the series solution by using a parabolic approximation [7]. Using the parabolic model of channel potential, we can

analytically solve the Schrödinger equation and derive the quantum-confinement model for UTB devices.

Threshold-voltage (V_T) roll-off is one of the most important signatures of SCEs, and hence V_T modeling will be a key step to estimate the degree of SCEs. For this purpose, the quantum electron density is needed to determine V_T for various UTB devices. So we calculate the quantum electron density by using the derived eigenenergies and eigenfunctions based on our quantum-confinement model.

V. P. Trivede and J. G. Fossum have demonstrated the quantum-mechanical effects on threshold-voltage of undoped double-gate (DG) MOSFET [8]. However, in their study, they only considered the long-channel devices. In other words, the channel potential of cross-section which experiences quantum confinement is always linear [9] and independent of channel length. Nevertheless, for short-channel devices, we have to consider the impact of SCEs on the channel potential distribution.

Since our parabolic channel potential model has included the dependence of channel length, the channel potential along the quantum-confinement direction will vary with the channel length. In other words, our quantum-confinement model based on the parabolic channel potential model can be used to assess the SCEs for UTB devices.

1.2 Organization

This thesis is organized as follows. In Chapter2, we present a parabolic channel

potential model of UTB MOSFETs with thin BOX under subthreshold region. In Chapter 3, the quantum-confinement model based on the parabolic channel potential model is derived and we discuss the impact of different channel materials and surface orientations on the degree of quantum confinement. In Chapter 4, we investigate the impact of quantum-mechanical effects on the V_T roll-off for GeOI devices. Chapter 5 is the conclusion of this thesis.
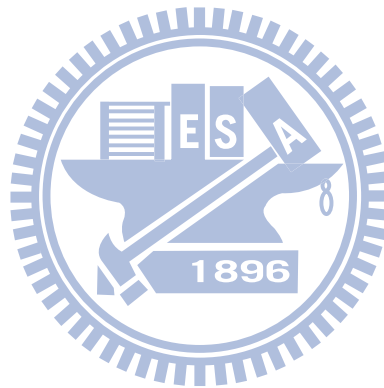
Chapter 2

Channel Potential Model for

Ultra-Thin-Body MOSFETs with Thin BOX

Under Subthreshold Region

2.1 Introduction

Ultra-thin-body (UTB) MOSFET with thin buried oxide (BOX) is a promising candidate to extend CMOS scaling because of its superior electrostatic integrity than bulk devices [10]-[12]. In addition, due to its better control of short-channel effects, lower subthreshold swing, and reduced leakage current, UTB MOSFET is also an ideal structure for the subthreshold circuit applications [13]. A channel potential model with series form for UTB MOSFETs under subthreshold region has been reported in [14]-[15]. Using the potential model, the electrostatic characteristics such as threshold-voltage, subthreshold swing, and subthreshold current can be estimated for various UTB devices.

To further simplify the series solution, in this chapter we present a compact form of model to be used in Chapter 3. The model verification is shown in Section 2.3. For various UTB structures with long- and short-channel length, thin- and thick-channel thickness, low and high channel doping concentration, and different buried oxide thickness, comparisons between the model and TCAD simulations have been carried out. Besides, we also examine the model at high and low drain biases and different back-gate biases.

2.2 Series Solution of Channel Potential

Our theoretical 2-D potential model for UTB MOSFETs is derived from the Poisson's equation. Fig. 2.1 shows a schematic sketch of a UTB device with thin buried oxide and silicon substrate. In the subthreshold region, the channel is fully depleted with negligible mobile carriers. Therefore, the channel potential distribution $\phi_{ch}(x, y)$ satisfies the Poisson's equation

$$\frac{\partial^2 \phi_{ch}(x,y)}{\partial x^2} + \frac{\partial^2 \phi_{ch}(x,y)}{\partial y^2} = -\frac{qN_{ch}}{\varepsilon_{ch}} \qquad (2.1)$$

, where N_{ch} and ε_{ch} are the channel doping concentration and permittivity, respectively. Since there is no charge in the buried oxide region, the buried oxide potential distribution $\phi_{BOX}(x, y)$ satisfies the Laplace equation

$$\frac{\partial^2 \phi_{BOX}(x,y)}{\partial x^2} + \frac{\partial^2 \phi_{BOX}(x,y)}{\partial y^2} = 0 \qquad (2.2)$$

The required boundary conditions can be described as [2.5]-[2.6]

$$\phi_{ch}(T_{ch}, y) + T_{ox} \frac{\varepsilon_{ch}}{\varepsilon_{ox}} \cdot \left. \frac{\partial \phi_{ch}(x,y)}{\partial x} \right|_{x=T_{ch}} = V_G - V_{FB} \qquad (2.3a)$$

$$\phi_{ch}(x, 0) = -\phi_{ms} + V_S \qquad (2.3b)$$

$$\phi_{ch}(x, L) = -\phi_{ms} + V_D \qquad (2.3c)$$

$$\phi_{BOX}(-T_{BOX}, y) = V_{back-gate} - V_{FB,back-gate} + \left(E_{i,ch} - E_{i,sub} \right) \qquad (2.3d)$$

$$\phi_{BOX}(x,0) = \left[V_{back-gate} - V_{FB,back-gate} + \left(E_{i,ch} - E_{i,sub}\right)\right]$$
$$+ x \cdot \frac{\left(-\phi_{ms} + V_S\right) - \left[V_{back-gate} - V_{FB,back-gate} + \left(E_{i,ch} - E_{i,sub}\right)\right]}{T_{BOX}} \quad (2.3e)$$

$$\phi_{BOX}(x,L) = \left[V_{back-gate} - V_{FB,back-gate} + \left(E_{i,ch} - E_{i,sub}\right)\right]$$
$$+ x \cdot \frac{\left(-\phi_{ms} + V_D\right) - \left[V_{back-gate} - V_{FB,back-gate} + \left(E_{i,ch} - E_{i,sub}\right)\right]}{T_{BOX}} \quad (2.3f)$$

$$\varepsilon_{ch} \cdot \left.\frac{\partial \phi_{ch}(x,y)}{\partial x}\right|_{x=0} = \varepsilon_{BOX} \cdot \left.\frac{\partial \phi_{BOX}(x,y)}{\partial x}\right|_{x=0} \quad (2.3g)$$

$$\left.\frac{\partial \phi_{ch}(x,y)}{\partial y}\right|_{x=0} = \left.\frac{\partial \phi_{BOX}(x,y)}{\partial y}\right|_{x=0} \quad (2.3h)$$

, where T_{ch}, T_{ox}, and T_{BOX} are the thicknesses of channel, gate oxide, and buried oxide, respectively. L is the gate length. ε_{ox} and ε_{BOX} are the permittivity of gate oxide and buried oxide, respectively. V_G, $V_{bacl-gate}$, V_S, and V_D are the voltage biases of gate, back-gate, source, and drain, respectively. V_{FB} and $V_{FB,back-gate}$ are the flat-band voltages of gate and back-gate, respectively. ϕ_{ms} is the built-in potential of the source/drain to the channel. $E_{i,ch}$ and $E_{i,sub}$ are the intrinsic Fermi level of channel and substrate, respectively.

The corresponding 2-D boundary value problem can be divided into two sub-problems, a 1-D Poisson's equation and a 2-D Laplace equation. Using the superposition principle, the complete channel potential solution is $\phi_{ch}(x,y) = \phi_{ch,1}(x) + \phi_{ch,2}(x,y)$, where $\phi_{ch,1}(x)$ and $\phi_{ch,2}(x,y)$ are the solutions of 1-D and 2-D sub-problems in the channel, respectively. The 1-D solution $\phi_{ch,1}(x)$ can be expressed as

$$\phi_{ch,1}(x) = -\frac{qN_{ch}}{2\varepsilon_{ch}}x^2 + A \cdot x + B \tag{2.4a}$$

$$A = \frac{(V_G - V_{FB}) - \left[V_{back-gate} - V_{FB,back-gate} + (E_{i.ch} - E_{i.sub})\right] + \frac{qN_{ch}}{2\varepsilon_{ch}}\left(T_{ch}^2 + 2\frac{\varepsilon_{ch}}{\varepsilon_{ox}}T_{ox}T_{ch}\right)}{T_{ch} + \frac{\varepsilon_{ch}}{\varepsilon_{ox}}T_{ox} + \frac{\varepsilon_{ch}}{\varepsilon_{BOX}}T_{BOX}}$$

$$\tag{2.4b}$$

$$B = \frac{\varepsilon_{ch}}{\varepsilon_{BOX}}T_{BOX} \cdot A + \left[V_{back-gate} - V_{FB,back-gate} + (E_{i,ch} - E_{i.sub})\right] \tag{2.4c}$$

In solving the 2-D sub-problem, the boundary condition of gate oxide/channel interface (2.3a) is simplified by converting the gate oxide dielectric thickness to $\varepsilon_{ch}/\varepsilon_{ox}$ times and replacing the gate oxide region with an equivalent channel-material region. The electric field discontinuity across the gate oxide and channel interface can thus be eliminated. For the channel/buried oxide interface, both the potential distribution in the channel ($\phi_{ch,2}(x, y)$) and that in the buried oxide ($\phi_{BOX,2}(x, y)$) have to be considered to satisfy the boundary conditions (2.3g) and (2.3h). The 2-D solution $\phi_{ch,2}(x, y)$ can be obtained using the method of separation of variables

$$\phi_{ch,2}(x, y) = \sum_n \left\{ \begin{array}{l} \left[c_n \cdot \sinh(\gamma_n y) + c_n' \cdot \sinh(\gamma_n(L - y))\right] \cdot \sin(\gamma_n x) \\ + e_n \cdot \sinh\left(\lambda_n\left(T_{ch} + \frac{\varepsilon_{ch}}{\varepsilon_{ox}}T_{ox} - x\right)\right) \cdot \sin(\lambda_n y) \end{array} \right\} \tag{2.5a}$$

, where

$$\lambda_n = (n\pi)/L \tag{2.5b}$$

$$\gamma_n = (n\pi)/(T_{ch} + (\varepsilon_{ch}/\varepsilon_{ox})T_{ox}) \tag{2.5c}$$

7

The coefficients c_n, $c_n^{'}$, and e_n in (2.5a) can be expressed as

$$c_n = \frac{1}{\sinh(\lambda_n L)}\left[\begin{array}{c} 2(\phi_{ms}+V_D-B)\cdot\dfrac{1-(-1)^n}{n\pi}+2A\left(T_{ch}+\dfrac{\varepsilon_{ch}}{\varepsilon_{ox}}T_{ox}\right)\cdot\dfrac{(-1)^n}{n\pi} \\[2ex] +2\left(T_{ch}+\dfrac{\varepsilon_{ch}}{\varepsilon_{ox}}T_{ox}\right)^2\cdot\dfrac{(-1)^n-1}{(n\pi)^3} \end{array}\right] \tag{2.5d}$$

$$c_n^{'} = \frac{1}{\sinh(\lambda_n L)}\left[\begin{array}{c} 2(-\phi_{ms}-B)\cdot\dfrac{1-(-1)^n}{n\pi}+2A\left(T_{ch}+\dfrac{\varepsilon_{ch}}{\varepsilon_{ox}}T_{ox}\right)\cdot\dfrac{(-1)^n}{n\pi} \\[2ex] +2\left(T_{ch}+\dfrac{\varepsilon_{ch}}{\varepsilon_{ox}}T_{ox}\right)^2\cdot\dfrac{(-1)^n-1}{(n\pi)^3} \end{array}\right] \tag{2.5e}$$

$$e_n = \frac{(RHS_n/LHS_n)}{\sinh\left((n\pi/L)\cdot(T_{ch}+(\varepsilon_{ch}/\varepsilon_{ox})T_{ox})\right)} \tag{2.5f}$$

, where

$$LHS_n = \lambda_n\cdot\coth(\lambda_n T_{BOX})+\frac{\varepsilon_{ch}}{\varepsilon_{BOX}}\lambda_n\cdot\coth(\lambda_n((\varepsilon_{ch}/\varepsilon_{ox})T_{ox}+T_{ch})) \tag{2.5g}$$

$$RHS_n = 2\frac{\varepsilon_{ch}}{\varepsilon_{BOX}}A\cdot\frac{1-(-1)^n}{n\pi}$$

$$+\sum_m\left\{\begin{array}{c}\left[c_n\cdot\dfrac{\dfrac{(2\varepsilon_{ch}/\varepsilon_{BOX})\cdot(-1)^{n+1}}{n\pi}\cdot\sinh(\lambda_m L)}{1+(\gamma_m/\lambda_n)^2}+c_n^{'}\cdot\dfrac{\dfrac{(2\varepsilon_{ch}/\varepsilon_{BOX})}{n\pi}\cdot\sinh(\lambda_m L)}{1+(\gamma_m/\lambda_n)^2}\right]\cdot\lambda_m \\[4ex] -d_n\dfrac{m\pi}{T_{BOX}}\dfrac{(-1)^{m+n+1}}{n\pi}\cdot\dfrac{2\sinh\left(\dfrac{m\pi}{T_{BOX}}L\right)}{1+(\gamma_m/\lambda_n)^2}-d_n^{'}\dfrac{m\pi}{T_{BOX}}\dfrac{(-1)^m}{n\pi}\cdot\dfrac{2\sinh\left(\dfrac{m\pi}{T_{BOX}}L\right)}{1+(\gamma_m/\lambda_n)^2}\end{array}\right\}$$

$$\tag{2.5h}$$

$$d_n = \frac{2}{\sinh(\gamma_n L)}\left\{\begin{array}{c}\left[V_{back-gate}-V_{FB,back-gate}+(E_{i,ch}-E_{i,sub})\right]\cdot\dfrac{1-(-1)^n}{n\pi} \\[2ex] +(-\phi_{ms}+V_D-B)\cdot\dfrac{(-1)^{n+1}}{n\pi}\end{array}\right\} \tag{2.5i}$$

$$d_n = \frac{2}{\sinh(\gamma_n L)} \left\{ \begin{array}{l} \left[V_{back-gate} - V_{FB,back-gate} + (E_{i,ch} - E_{i,sub}) \right] \cdot \frac{1-(-1)^n}{n\pi} \\ + (-\phi_{ms} - B) \cdot \frac{(-1)^{n+1}}{n\pi} \end{array} \right\} \tag{2.5j}$$

Based on the potential solution, the subthreshold current (for nMOSFETs) can also be derived [16] by

$$I_{DS} = \frac{W\mu_n kT(n_i^2/N_A) \cdot [\exp(-qV_S/kT) - \exp(-qV_D/kT)]}{\int_0^L dy \Big/ \int_0^{T_{ch}} \exp[q\phi_{ch}(x,y)/kT]dx} \tag{2.6}$$

2.3 Compact Form and Verification

2.3.1 Compact Form

From equations (2.4) and (2.5), we can obtain the classical potential in whole channel [2.5]-[2.6]. However, the series solution is too complicated to be used in solving the Schrödinger equation in Chapter 3. To simplify the solution, the potential in the channel $\phi_{ch}(x,y)$ is further reduced to a parabolic form. Since the direction of quantum confinement is perpendicular to the interface between oxide and channel, we express the channel potential along the x-direction for each slice of y-direction as

$$\phi_{ch}(x) = \sum_{i=0}^{2} f_i \cdot \prod_{\substack{j=0 \\ j \neq i}}^{2} \frac{(x-x_j)}{(x_i-x_j)} \tag{2.6}$$

, where f_i is the channel potential obtained from series solution and x_i is the corresponding location. In fact, equation (2.6) is the Lagrange interpolating

polynomial of degree 2 that passes three points. If the three points are determined, the equation (2.6) can be expressed as the parabolic form

$$\phi_{ch}(x) = a_2 x^2 + a_1 x + a_0 \qquad (2.7)$$

, where a_2, a_1, and a_0 can be calculated from equation (2.6).

So the next issue is to choose the three points that can make the parabolic form faithfully represent the series solution. We propose a methodology to determine the three points, and the methodology obeys the following principles:

1. The three points contain the highest potential and another two boundaries along the x-direction.

2. If the highest potential is also the boundary, we choose the midpoint and the other boundary along the x-direction.

The reason why we choose the highest potential is that the carrier flow (electron flow in NMOS) may be the largest through this point. In the words, the point is critical to the determination of electron density and subthreshold current. Using the methodology, we can reconstruct the channel potential by the compact form instead of series solution. Notice that the sets of a_2, a_1, and a_0 will be different if we choose different cross-sections of y-direction.

Comparisons between the compact parabolic form and series solution are shown in Fig 2.2. It shows that the reduced parabolic form is fairly accurate with L=30nm and 15nm and V_{DS}=0.05V and 1V for Ge-channel devices. The curves of compact model in the y-direction are slightly discontinuous since we only reduce the channel potential along the x-direction. In the following verification, we will use the compact

form instead of series solution.

2.3.2 Verification

We use Ge-channel devices in the model verification. The channel length (L) is 30nm and 15nm, the gate oxide thickness (T_{ox}) is 1nm, the channel thickness (T_{ch}) is 5nm and 10nm, the buried oxide thickness (T_{BOX}) is 1nm, 5nm and 10nm. The drain bias (V_{DS}) is 0.05V and 1V and the back-gate bias (V_{BS}) is 0V, 0.2V, and 0.5V. The channel doping concentration (N_A) is 1×10^{15} cm^{-3} and 1×10^{18} cm^{-3}. Besides, we use the heavily-doped (1×10^{20} cm^{-3}) silicon substrate and treat it as ground plane.

Fig. 2.3 shows the potential distribution across half T_{ch} and half L in the long- and short-channel devices and in the thin- and thick-channel thickness devices for model and TCAD results. It shows that our model is fairly accurate for various channel sizes. In Fig 2.4, our model is suitable for different channel doping concentrations (N_A). In Fig 2.5, our model is also satisfactory for T_{BOX} =1nm and 5nm and implies that the model may be applied for double-gate (DG) devices when $T_{ox} = T_{BOX}$. Fig 2.6 shows the potential distribution at high and low drain biases (V_{DS}) and at different back-gate biases (V_{BS}). The model is also accurate compared with TCAD simulations. The compact parabolic potential model shows excellent agreement with TCAD simulations for UTB devices.

2.4 Summary

We have developed a channel potential model for UTB MOSFETs under subthreshold region. Specifically, we propose a compact form of model instead of

series solution. To examine the accuracy of the compact parabolic model, we have carried out extensive verification for various L, T_{ch}, N_A, T_{BOX}, V_{DS}, and V_{BS}. All verification results show sufficient accuracy compared with TCAD simulations. The compact form not only makes the expression of potential model clear but also simplify the derivation of eigenenergy (E_n) and eigenfuction (ψ_n). That will be discussed in Chapter 3.
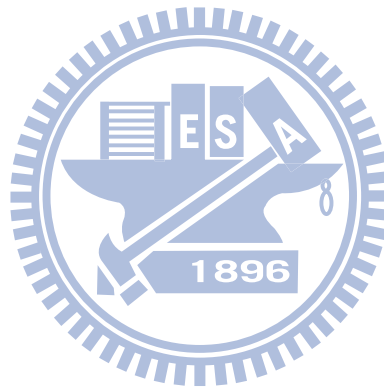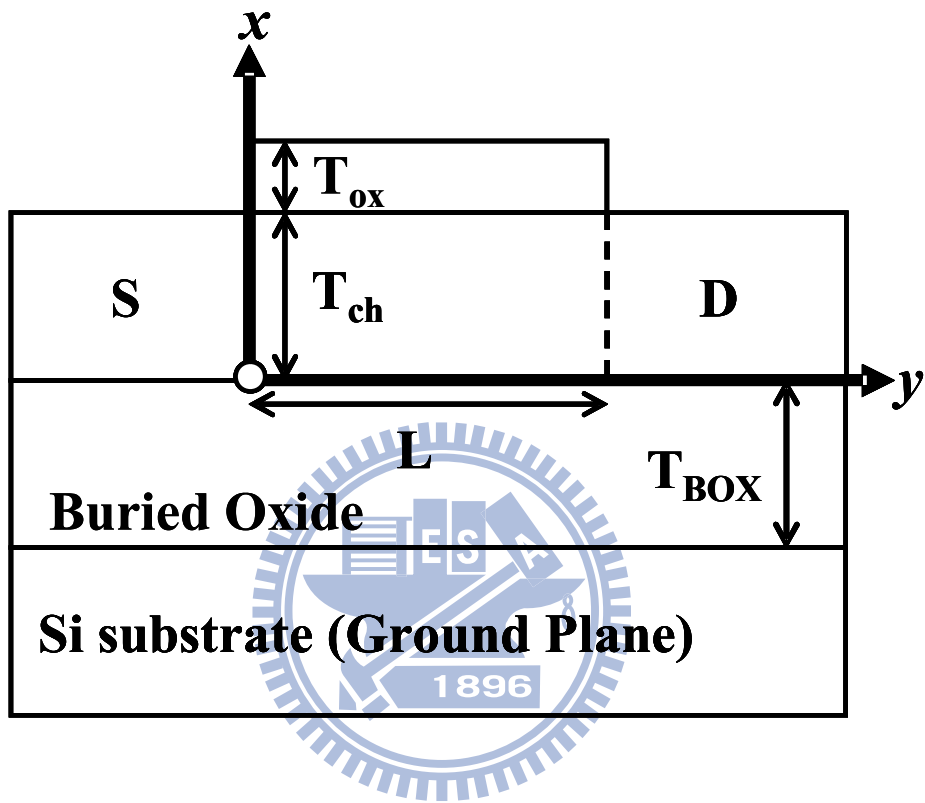
Fig. 2.1 Schematic sketch of the UTB structure investigated in this study.
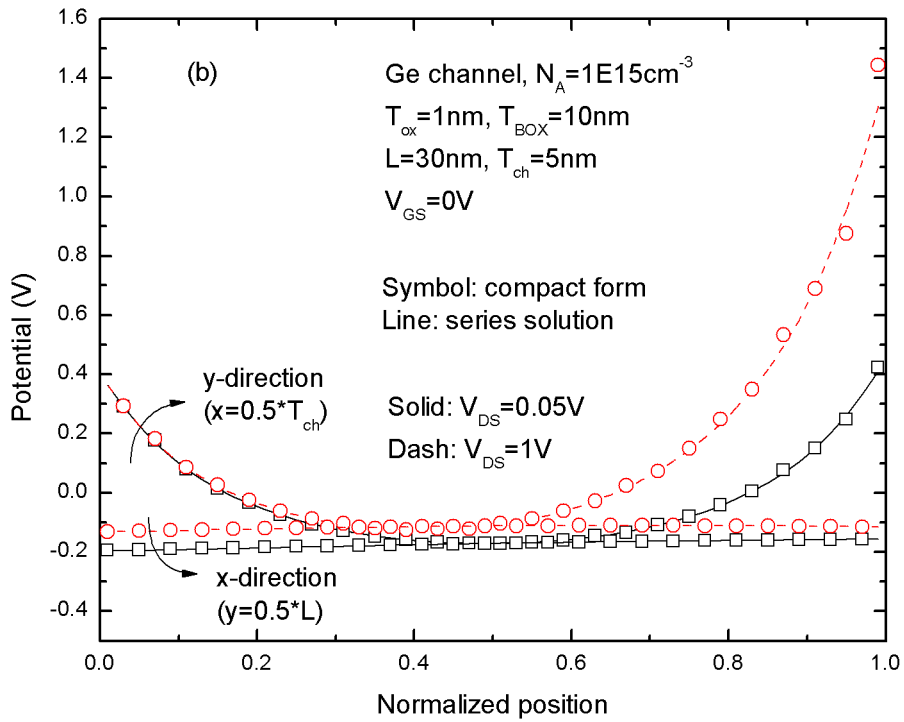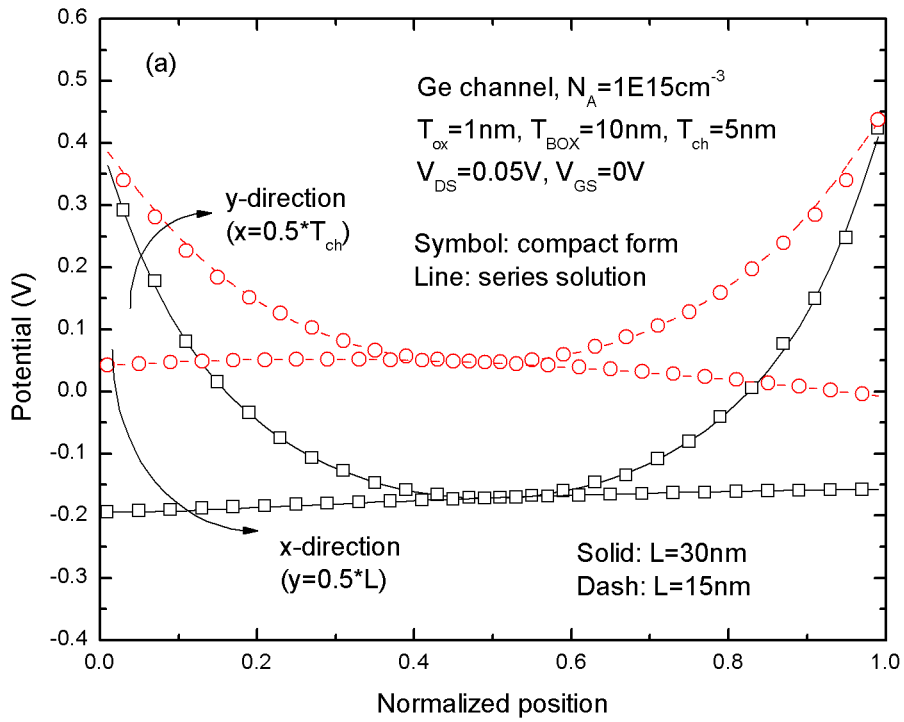
Fig. 2.2 Potential distribution for UTB devices with (a) L =30nm and 15nm and

of (b) V_{DS} =0.05V and 1V using model in compact form and series solution.
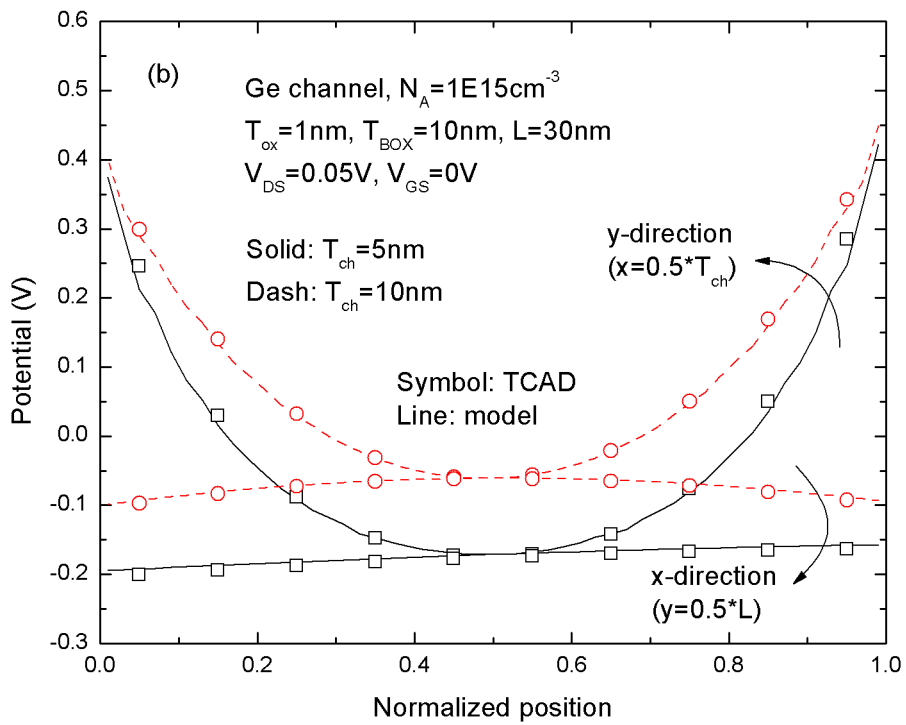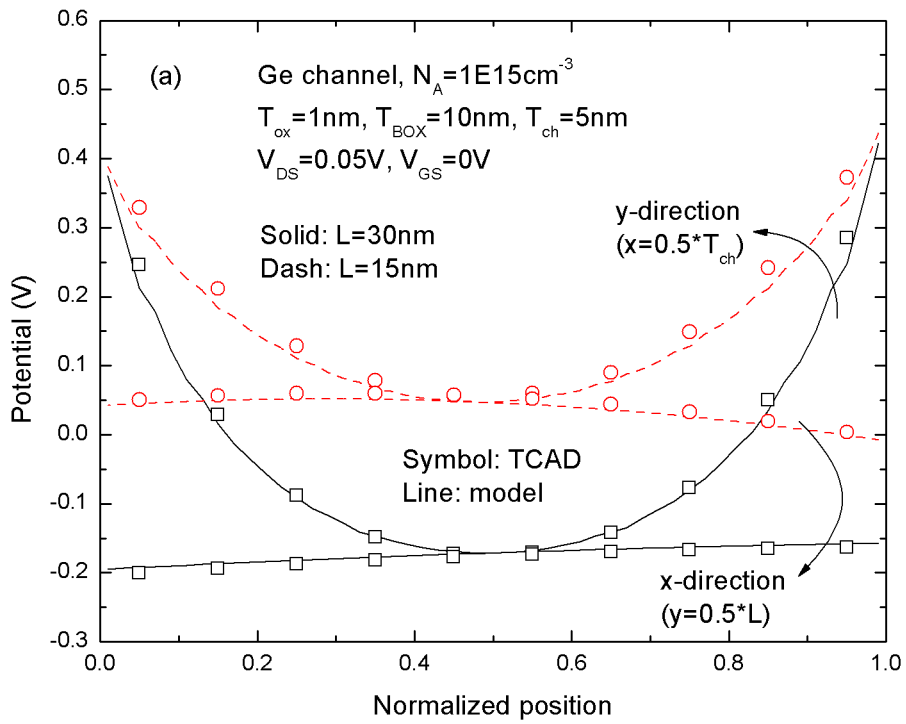
Fig. 2.3 Potential distribution for UTB devices with (a) L =30nm and 15nm, and (b) T_{ch} =5nm and 10nm using model and TCAD simulation.
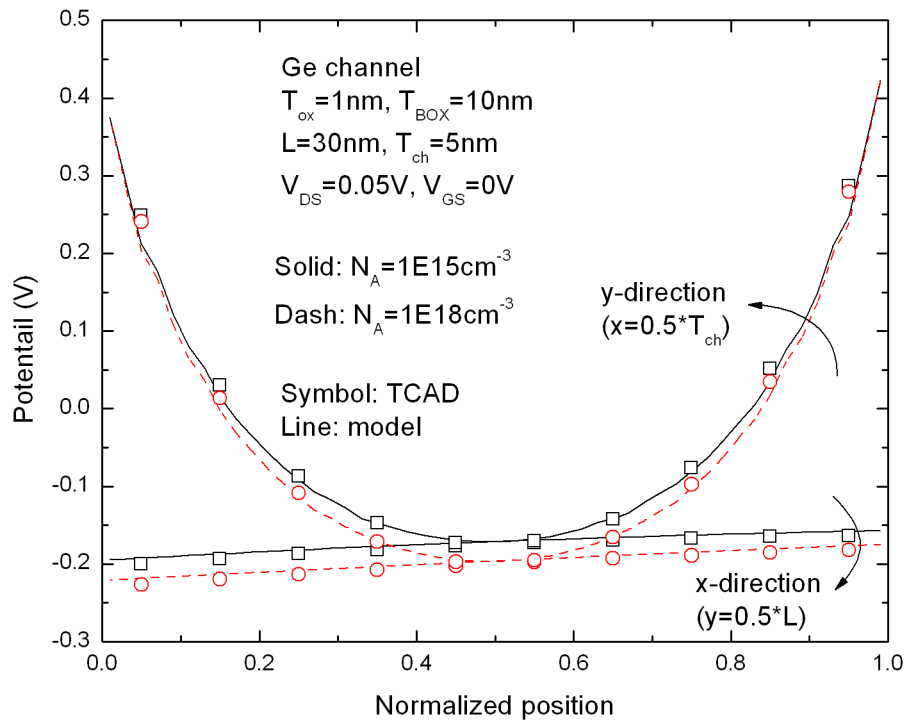
Fig. 2.4 Potential distribution for UTB devices with $N_A = 1 \times 10^{15}$ cm^{-3}, and $N_A = 1 \times 10^{18}$ cm^{-3} using model and TCAD simulation.
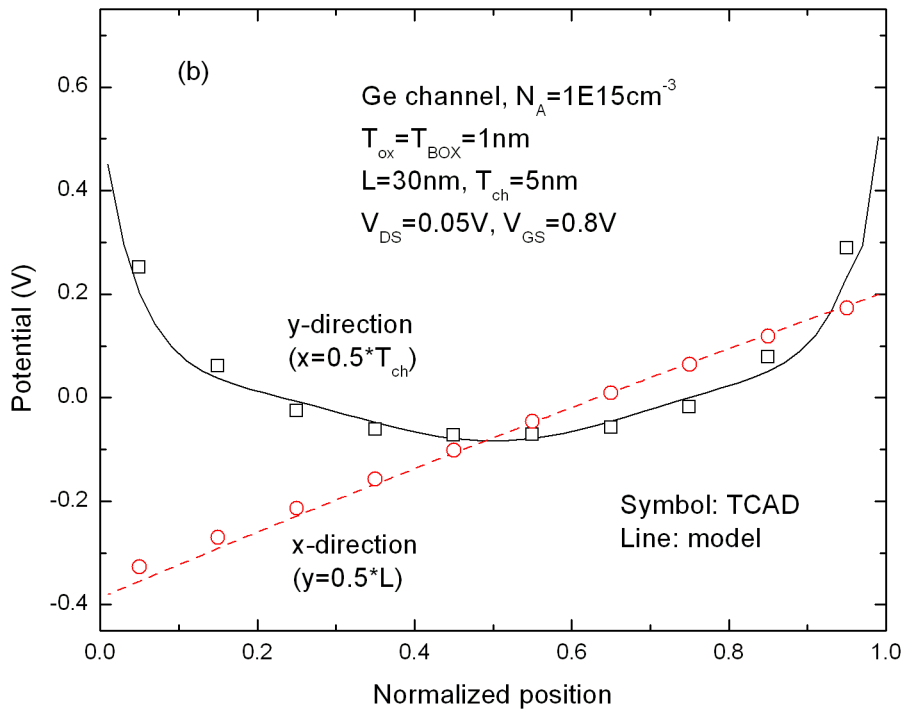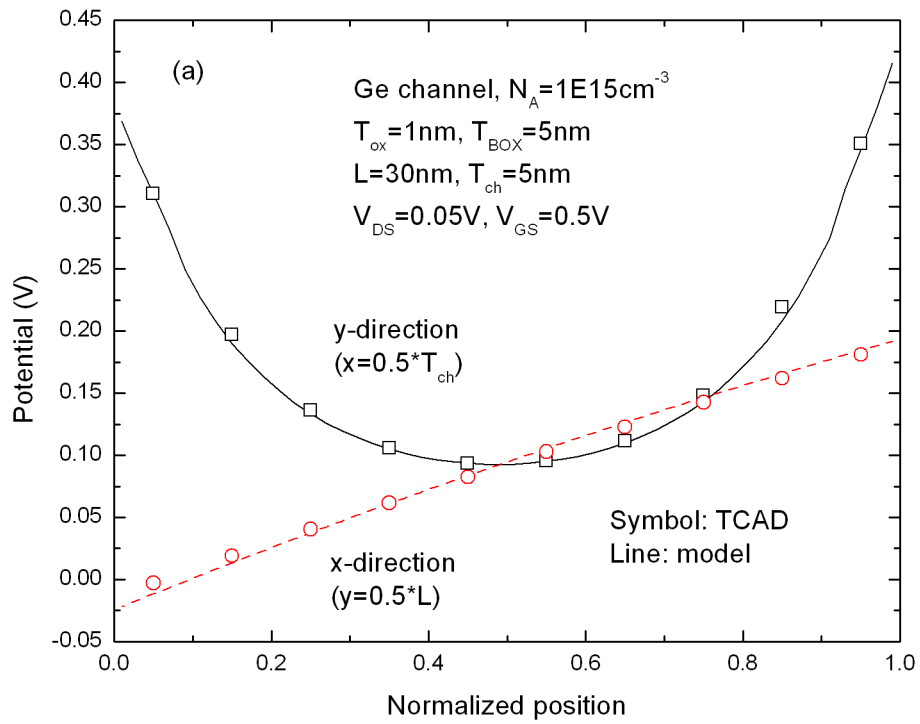
Fig. 2.5 Potential distribution for UTB devices with (a) T_{BOX} =5nm, and (b)

T_{BOX} =1nm using model and TCAD simulation.
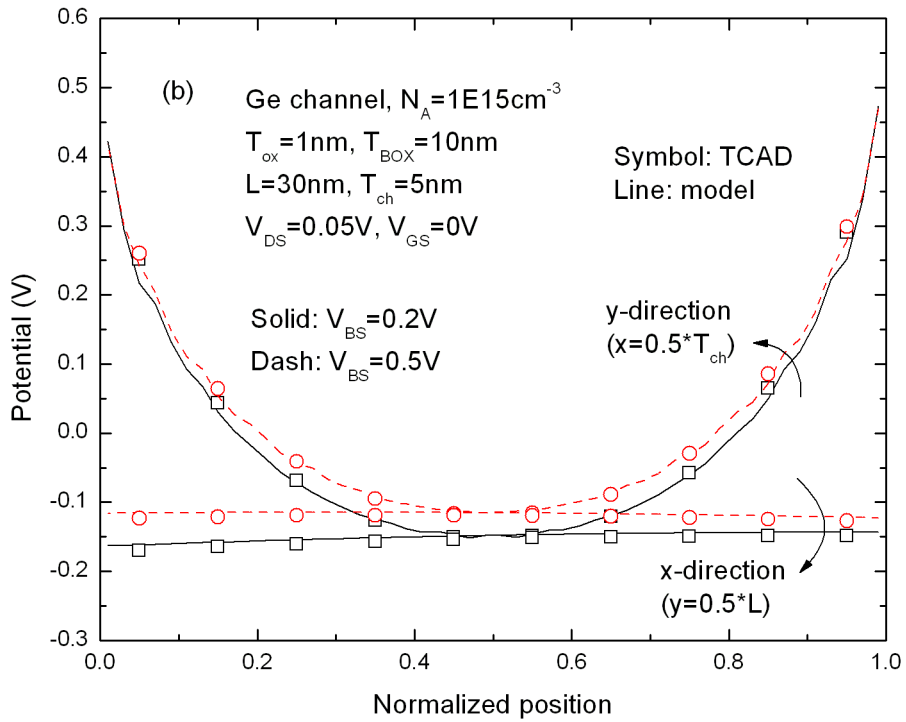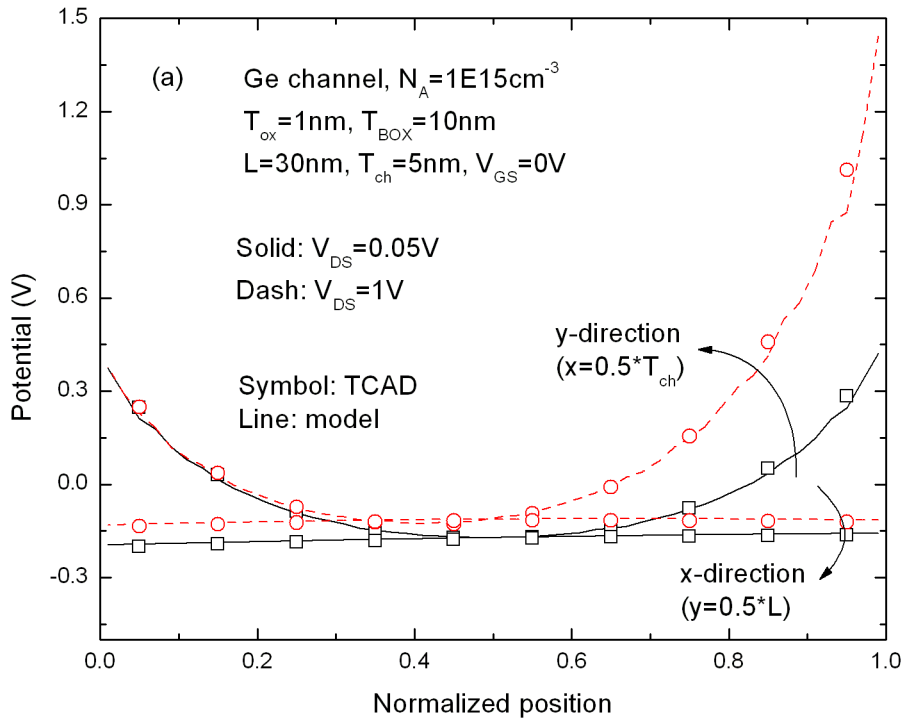
Fig. 2.6 Potential distribution for UTB devices with (a) V_{DS} =0.05V and 1V, and

(b) V_{BS} =0.2V and 0.5V using model and TCAD simulation.

18

Chapter 3

Quantum-Confinement Model for

Ultra-Thin-Body MOSFETs with Thin BOX

Under Subthreshold Region

3.1 Introduction

With decreasing channel thickness, quantum-confinement effect may be significant [17]-[18] and may affect the electrostatic characteristics of ultra-thin-body (UTB) MOSFETs [19]. In this chapter, an analytical solution of the Schrödinger equation for UTB MOSFETs under subthreshold region is presented. Based on the parabolic channel potential model developed in Chapter 2, we derive the eigenenergy and eigenfunction of UTB devices. Therefore, the electron density in the channel considering quantum mechanism can be obtained by using the calculated eigenenergy and eigenfunction. Besides, we also discuss the impacts of channel material and surface orientation [20]-[21]. Quantum-mechanical effects on Si-, Ge-, and In$_{0.53}$Ga$_{0.47}$As-channel UTB devices will be assessed.

3.2 Model Derivation

The eigenenergy and eigenfunction of channel carriers are crucial to the quantum-mechanical effects, and they can be determined by solving the Schrödinger equation [3.6]. The schematic sketch of a UTB device has been shown in Fig 2.1. Because the direction of quantum confinement (x) is perpendicular to the interface

between oxide and channel, for each cross-sections of y-direction, the Schrödinger equation for the UTB devices can be expressed as

$$-\frac{\hbar^2}{2m_x^*}\frac{\partial}{\partial x^2}\psi_n(x) + E_C(x)\cdot\psi_n(x) = E_n\cdot\psi_n(x) \tag{3.1}$$

, where E_n is the eigenenergy, $\psi_n(x)$ is the corresponding wavefunction, $\hbar$ is the reduced Plank constant, m_x^* the effective mass of electron perpendicular to the interface between oxide and channel, and $E_C(x)$ is the conduction band edge.

In Chapter 2, we have proposed a compact form of the channel potential $\phi_{ch}(x) = a_2 x^2 + a_1 x + a_0$ (equation (2.7)). Besides, the conduction band edge can be expressed as

$$E_C(x) \equiv -q\cdot\phi_{ch}(x) + \frac{1}{2}E_g - \frac{1}{2}\frac{kT}{q}\cdot\ln\left(\frac{N_V}{N_C}\right) \tag{3.2}$$

, where E_g is the band gap of channel material, N_V is the effective density of states in the conduction band, and N_C is the effective density of states in the valence band, respectively. Therefore, from equation (2.7) and equation (3.2), the conduction band edge can be expressed as

$$E_C(x) = a_2'x^2 + a_1'x + a_0' \tag{3.3}$$

, where a_2', a_1', and a_0' are known values and can be obtained from the parabolic channel potential model presented in Chapter 2.

Using equation (3.3), equation (3.1) can be expressed as

$$\frac{\partial^2}{\partial x^2}\psi_n(x) + \frac{2m^*}{\hbar^2}\left[E_n - \left(a_2' x^2 + a_1' x + a_0'\right)\right] \cdot \psi_n(x) = 0 \qquad (3.4)$$

If we use the power series method and assume

$$\psi_n(x) = \sum_{i=0}^{\infty} c_i x^i \qquad (3.5a)$$

, the coefficients c_i can be determined by the following recurrence relationship [22]

$$c_2 = \frac{m_x^*}{\hbar^2}\left(a_0' - E_n\right) \cdot c_0 \qquad (3.5b)$$

$$c_3 = \frac{m_x^*}{3\hbar^2}\left[\left(a_0' - E_n\right) \cdot c_1 + a_1' \cdot c_0\right] \qquad (3.5c)$$

$$c_i = \frac{2m_x^*}{i(i-1)\hbar^2}\left[\left(a_0' - E_n\right) \cdot c_{i-2} + a_1' \cdot c_{i-3} + a_2' \cdot c_{i-4}\right] , \ i \geq 4 \qquad (3.5d)$$

The required boundary conditions can be described as

$$\psi_n(x = 0) = 0 \qquad (3.6a)$$

$$\psi_n(x = T_{ch}) = 0 \qquad (3.6b)$$

$$\int_0^{T_{ch}} |\psi_n(x)|^2 \, dx = 1 \qquad (3.6c)$$

From equation (3.6a), we know that $c_2 = c_0 = 0$. Then c_1 can be derived from equation (3.6c) and the eigenenergy E_n can be obtained by equation (3.6b). Thus, the eigenfunction $\psi_n(x)$ for UTB devices under subthreshold region can be derived. Generally, 60 terms in the summation of (3.5a) are needed to give sufficiently accurate results.

Using Fermi-Dirac statistics, the discrete nature of the quantized density of states reduces the integral over energy to a sum over bound state energies [23]. Besides, since we consider the quantum-confinement effect and possibly different types of valleys, the expression for the electron density then becomes [24]

$$n(x,y) = \sum_{v}\left\{ \frac{d_v m_{d,v} kT}{\pi\hbar^2} \cdot \sum_{n}\left[\ln\left(1 + \exp\left(\frac{E_F(y) - E_{n,v}}{kT}\right)\right) \cdot |\psi_{n,v}(x,y)|^2 \right]\right\} \qquad (3.5)$$

, where v is the type of valley, d_v is the degeneracy of the valley, $m_{d,v}$ is the effective density-of-state mass of the valley, and $E_F(y)$ is the quasi-Fermi level in the channel along the y-direction.

In equation (3.5), the $\exp((E_F(y) - E_{n,v})/kT)$ term is usually much smaller than 1 under subthreshold region. So we can further approximate the equation (3.5) as

$$n(x,y) = N_{C,QM}(x,y) \cdot \exp\left(\frac{E_F(y) - E_C(x,y)}{kT}\right) \qquad (3.6a)$$

$$\text{with} \quad N_{C,QM}(x,y) = \frac{kT}{\pi\hbar^2} \cdot \sum_{v}\left[d_v \cdot m_{d,v} \cdot \sum_{n}\left(\exp\left(\frac{E_C(x,y) - E_{n,v}}{kT}\right) \cdot |\psi_{n,v}(x,y)|^2 \right)\right]$$

$$(3.6b)$$

3.3 Verification and Discussion

In Fig 3.1, we compare the conduction band edge and corresponding eigenenergies between long- and short-channel devices as T_{ch}=10nm. It shows that the shape of the conduction band edge depends on the channel length. The $(E_1 - E_{C,\min})$s are about 0.1eV for the long-channel device and about 0.06eV for the

short-channel one. That is, the degree of quantization is affected by the conduction band edge with different channel length when T_{ch}=10nm.

Fig 3.2 shows the calculated quantized n th eigenenergy (E_n) in Ge-channel devices with various T_{ch}. We can find that as T_{ch}=5nm, $(E_2 - E_1) \approx 0.35 eV$ is much larger than $kT = 0.026 eV$. From equation (3.6), it can be expected that the first eigenenergy (E_1) will be dominant in the determination of the electron density when quantum-confinement effect is strong.

In Fig. 3.3, we show the square of the first eigenfunction ($|\psi_1|^2$) with T_{ch}=5nm and 10nm. Fig 3.4 shows the electron density across half L for the UTB devices. Although the square of the first eigenfunction with T_{ch}=5nm is larger than the one with T_{ch}=10nm, the electron density with T_{ch}=5nm is smaller than the one with T_{ch}=10nm as shown in Fig 3.4. From equation (3.6), the T_{ch}=5nm UTB device is expected to have smaller electron density since it possess large $(E_1 - E_{C,min})$ as shown in Fig 3.2. Our quantum-mechanical model is fairly accurate compared with TCAD simulations.

3.4 Various Channel Materials and Surface Orientations

Changing channel materials may improve device performance through the enhancement of carrier mobility. In this chapter, we will use Si, Ge, and In$_{0.53}$Ga$_{0.47}$As as channel materials to examine our quantum-mechanical model. In addition, since Si and Ge have three common surface orientations (100), (110), and (111), we will discuss the impact of surface orientation considering quantum mechanism.

To consider quantum mechanism, the first thing is that different channel material or surface orientation may have different corresponding effective mass (m_x^*). The effective mass will determine the degree of quantization. The channel with lighter effective mass will have stronger quantum-mechanical effects. For a given surface orientation, Si or Ge may have two distinct effective masses with corresponding degeneracy (d_v) and effective density-of-state mass ($m_{d,v}$). Table 3.1 shows m_x^*, d_v, and $m_{d,v}$ of the three channel materials considering various surface orientations [24]-[26].

In this work, we use our parabolic channel potential model for different channel materials. Then based on our quantum-mechanical model, we can use the parameters in Table 3.1 to solve the Schrödinger equation and to calculate the electron density considering the impact of surface orientation.

Fig 3.5 shows the channel potentials of Si and In$_{0.53}$Ga$_{0.47}$As, respectively. It can be seen that our parabolic channel potential model is accurate. Fig. 3.6 shows the $\left(E_1 - E_{C,\min}\right)$ for Si with (100) and (110) surface orientations. Because these orientations have two types of valley (two effective mass m_x^*), there exists two $\left(E_1 - E_{C,\min}\right)$. We can find that the difference between the two $\left(E_1 - E_{C,\min}\right)$ becomes large ($\gg kT = 0.026eV$) when T_{ch} about 3nm. It means that the valley with smaller $\left(E_1 - E_{C,\min}\right)$ will determine the electron density in ultrathin T_{ch} devices. Similarly, Fig 3.7 shows the $\left(E_1 - E_{C,\min}\right)$ for Ge with (110) and (111) surface orientations.

24

When T_{ch} about 5nm, the difference becomes obvious and hence we can treat the valley with smaller $\left(E_1 - E_{C,\min}\right)$ as the dominant type for calculating the electron density. From Fig 3.6 and Fig 3.7, we can find that in ultrathin T_{ch} devices ($T_{ch} \approx 3$nm for Si, $T_{ch} \approx 5$nm for Ge), the type of valley with heavier effective mass will determine the electron density.

Table 3.2 collects the critical effective masses ($m^*_{x,crit}$) which dominate the electron density. The table can help us understand what critical effective mass may affect the degree of quantization and corresponding electrostatic characteristics in ultrathin T_{ch} devices. Fig 3.8 shows the dominant $\left(E_1 - E_{C,\min}\right)$ of Si-channel with (100) orientation, Ge-channel with (100) orientation, and In$_{0.53}$Ga$_{0.47}$As-channel UTB devices, respectively. We can find that the In$_{0.53}$Ga$_{0.47}$As-channel UTB device has the largest $\left(E_1 - E_{C,\min}\right)$ and thus experiences the strongest quantum-mechanical effects.
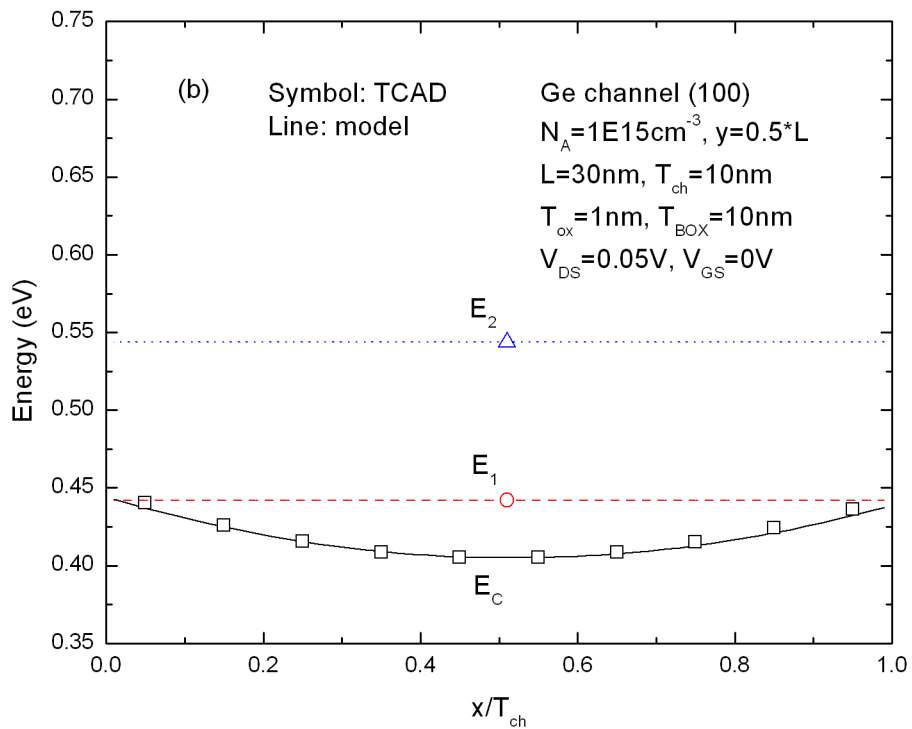
Fig. 3.9 shows the square of the first eigenfunction ($\left|\psi_1\right|^2$) for Si- and In$_{0.53}$Ga$_{0.47}$As-channel UTB devices. Note that Si-channel UTB device with (100) orientation has two types of $\left|\psi_1\right|^2$. In Fig 3.10, we show the electron density for different channel materials in the UTB devices. It can be seen that for Si-channel UTB device with (100) orientation, the electron density of the dominant type of valley (2-fold valley) essentially determines the total electron density for the T_{ch}=5nm device. This supports our use of the critical effective mass to determine the degree of quantization.

3.5 Summary

In this chapter, we present the UTB MOSFET model considering quantum mechanism based on our previous parabolic channel potential model. Using the model, we can obtain eigenergy, eigenfuction, and quantum electron density. Besides, we have demonstrated that $\left(E_1 - E_{C,\min}\right)$ will be the dominant term to determine the electron density, especially for ultrathin T_{ch} devices.

We have also discussed the impacts of different channel materials and surface orientations considering quantum mechanism. We find that the channel material which experiences the strongest quantum-mechanical effects has the lightest effective mass (m_x^*). We have constructed the table (Table 3.2) of the critical effective masses ($m_{x,crit}^*$) which determine the degree of quantum confinement.
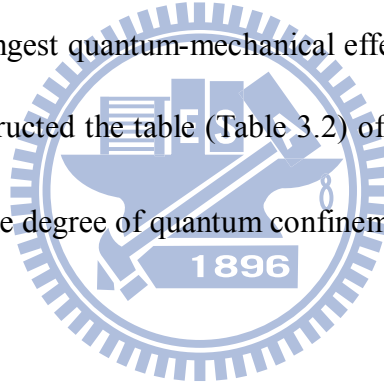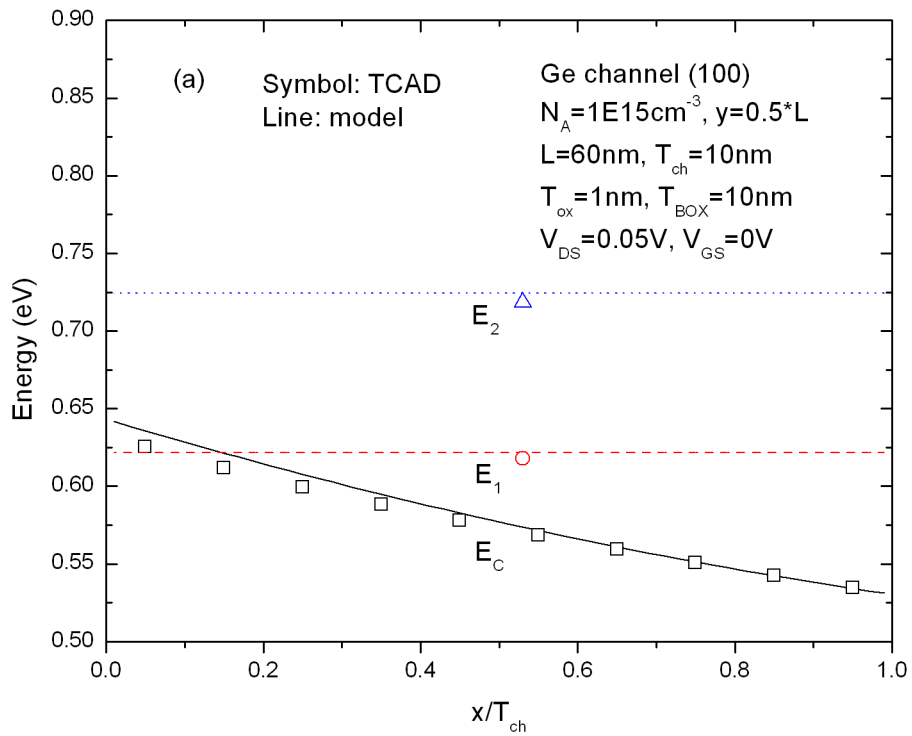
Fig. 3.1 The conduction band edge and corresponding eigenenergies for
T_{ch}=10nm devices with (a) L=60nm and (b) L=30nm.
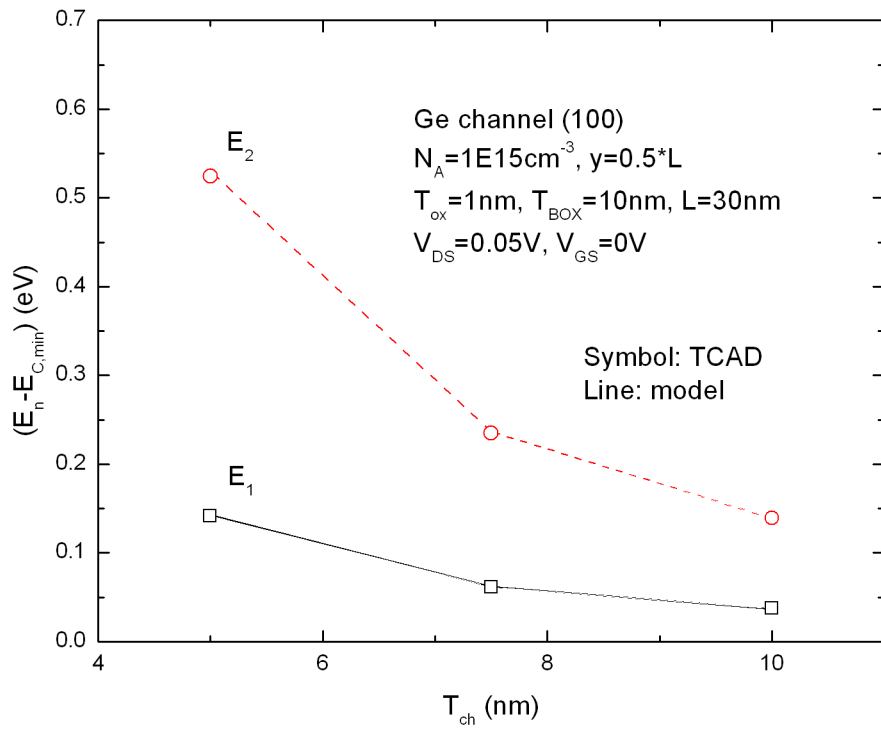
Fig. 3.2 The calculated quantized n th eigenenergy (E_n) for the devices with various T_{ch} .
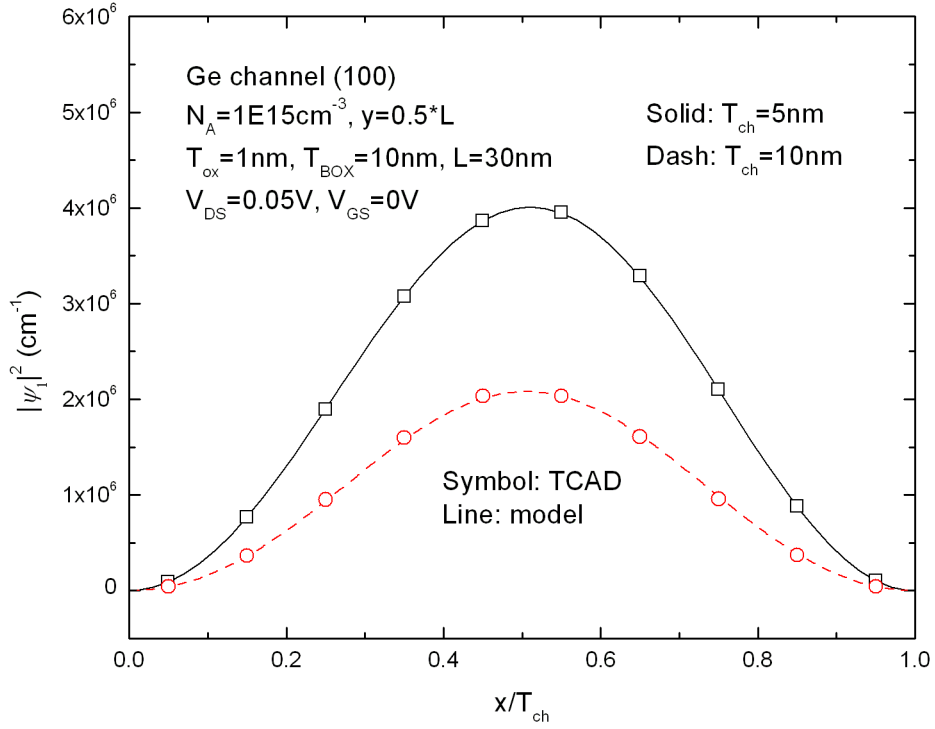
Fig. 3.3 The square of the first eigenfunction ($\left| \psi_1 \right|^2$) for T_{ch}=5nm and 10nm in the Ge-channel UTB devices.
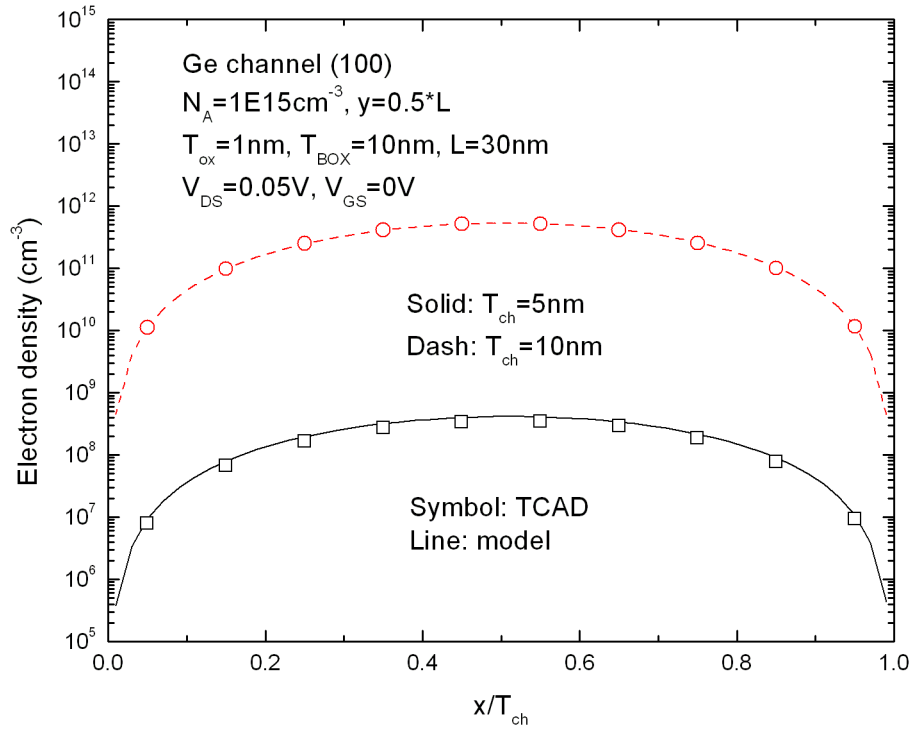
Fig. 3.4 The electron density for T_{ch}=5nm and 10nm in the Ge-channel UTB devices.

Table 3.1 m_x^*, d_v, and $m_{d,v}$ of three channel materials considering surface orientations. m_0 is the free electron mass 9.11×10^{-31} kg. [24]-[26]

		(100)	(110)	(111)
Si	m_x^*	$0.916\,m_0$ $0.191\,m_0$	$0.316\,m_0$ $0.191\,m_0$	$0.259\,m_0$
	d_v	2 4	4 2	6
	$m_{d,v}$	$0.191\,m_0$ $0.418\,m_0$	$0.325\,m_0$ $0.418\,m_0$	$0.359\,m_0$
Ge	m_x^*	$0.117\,m_0$	$0.218\,m_0$ $0.08\,m_0$	$1.57\,m_0$ $0.0894\,m_0$
	d_v	4	2 2	1 3
	$m_{d,v}$	$0.293\,m_0$	$0.215\,m_0$ $0.354\,m_0$	$0.08\,m_0$ $0.335\,m_0$
In$_{0.53}$Ga$_{0.47}$As	m_x^*	$0.041\,m_0$		
	d_v	1		
	$m_{d,v}$	$0.041\,m_0$		
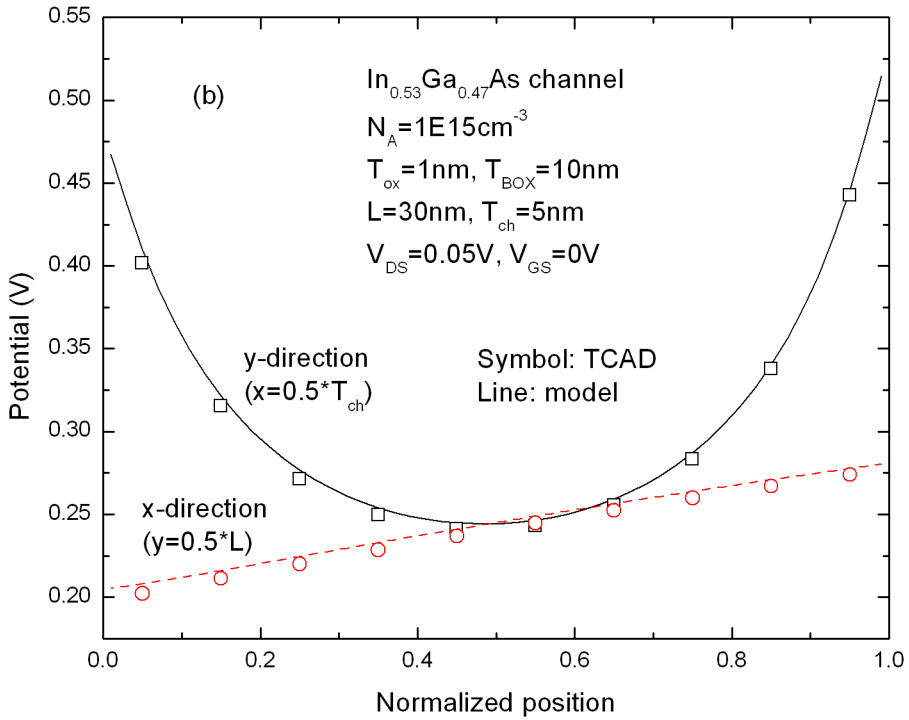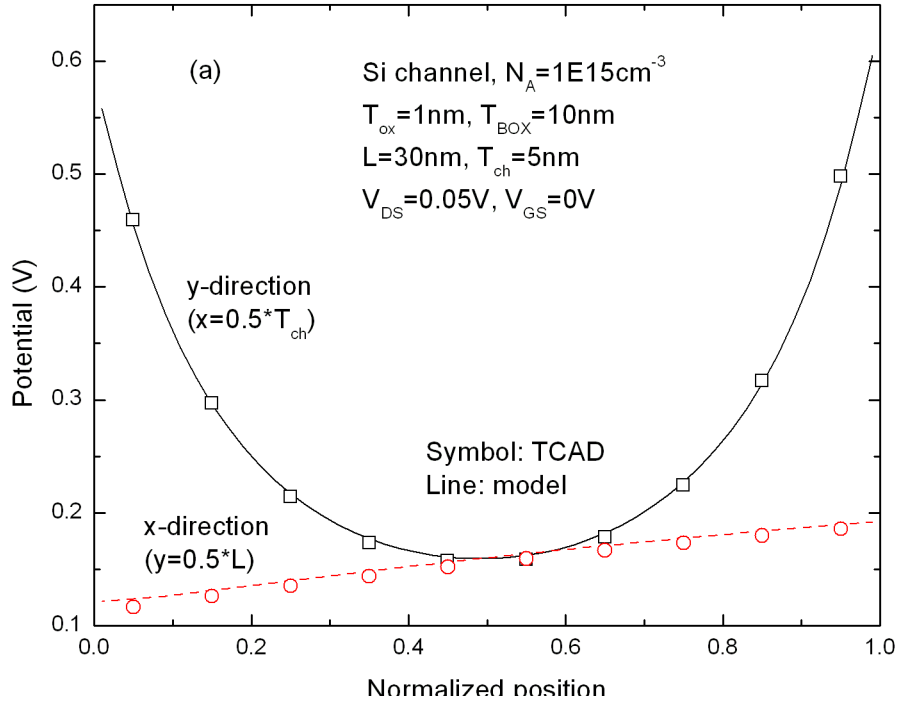
Fig. 3.5 The potential distribution of (a) Si-channel UTB device, and (b) $In_{0.53}Ga_{0.47}As$-channel UTB device for model and TCAD results.
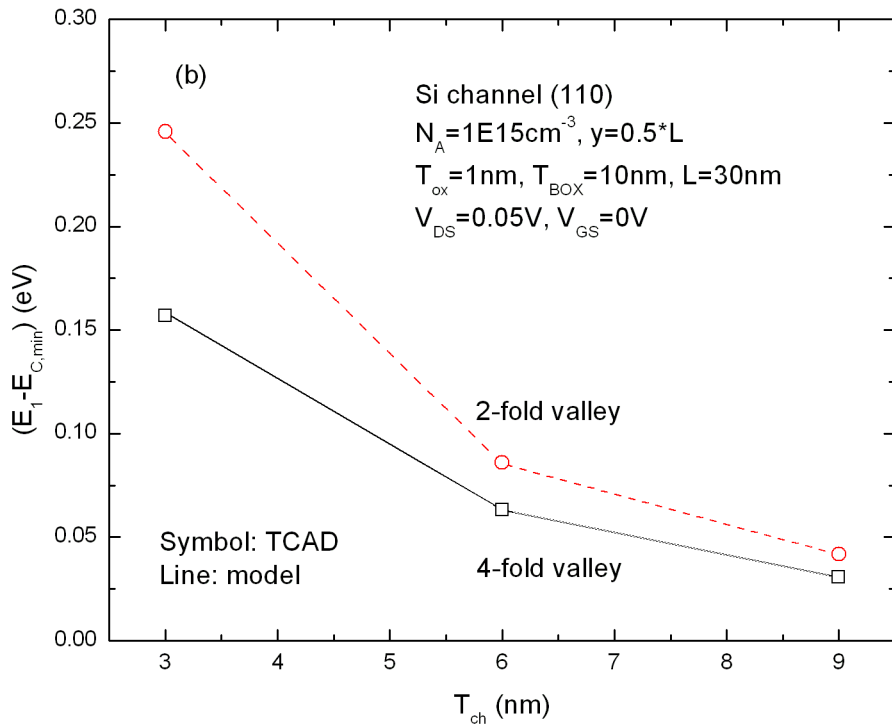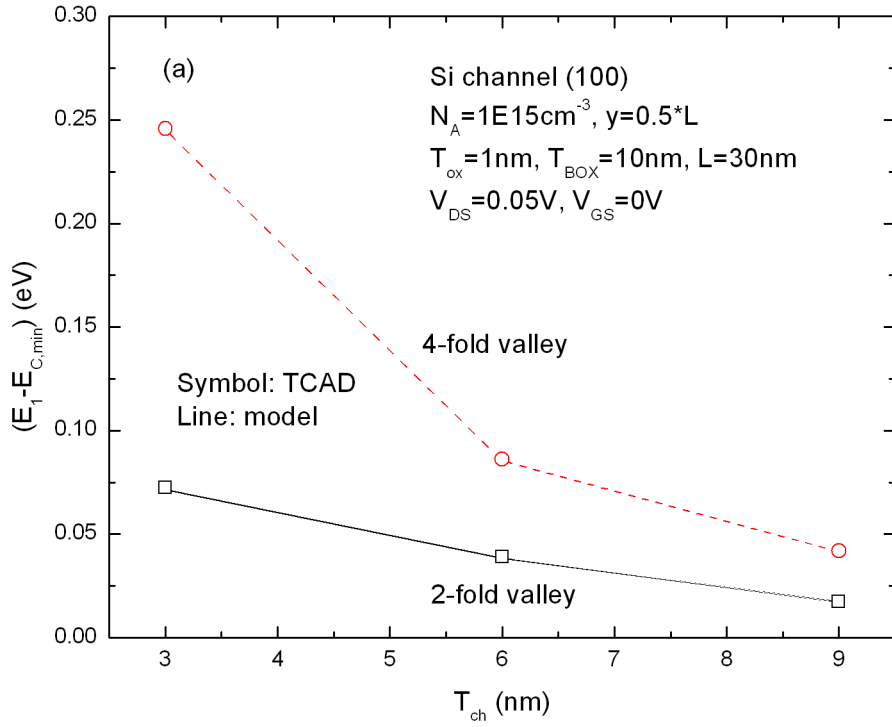
Fig. 3.6 The $\left(E_1 - E_{C,\min}\right)$ of Si-channel UTB devices with (a) (100) and (b) (110)

surface orientations with model and TCAD results.

32
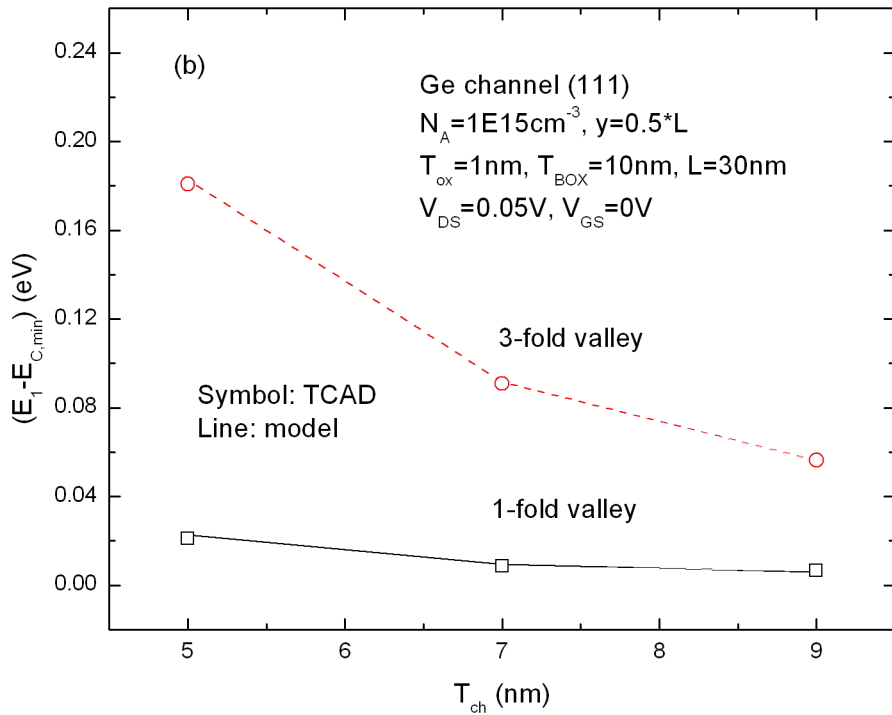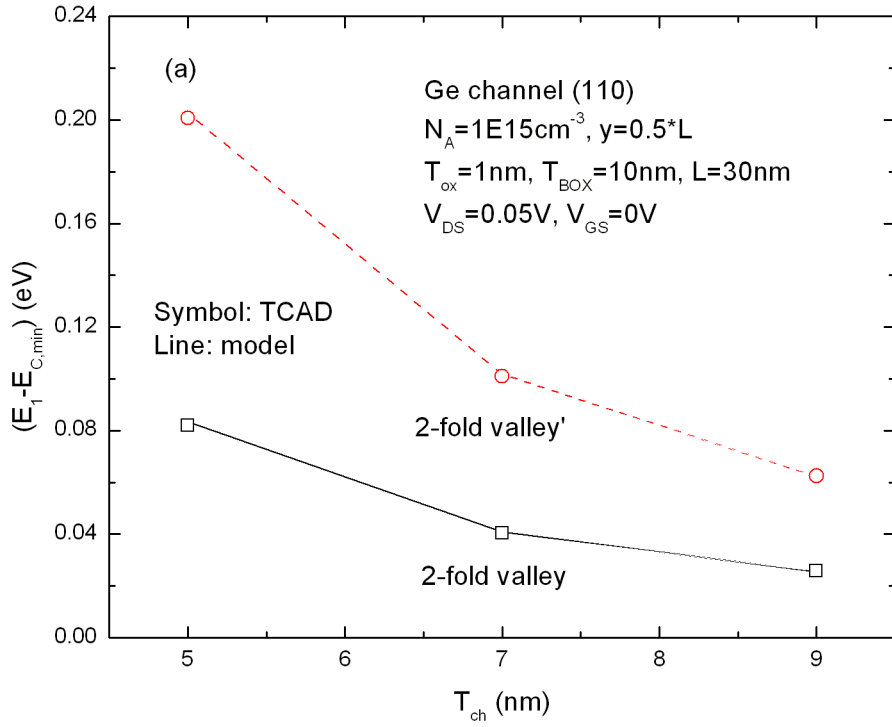
Fig. 3.7 The $\left(E_1 - E_{C,\min} \right)$ of Ge-channel UTB devices with (a) (110) and (b)

(111) surface orientations with model and TCAD results.

Table 3.2 The critical $m_{x,crit}^*$ of three channel materials considering surface orientations when quantum-mechanical effect is strong in ultrathin T_{ch} devices.

		(100)	(110)	(111)
Si	$m_{x,crit}^*$	$0.916\,m_0$	$0.316\,m_0$	$0.259\,m_0$
Ge	$m_{x,crit}^*$	$0.117\,m_0$	$0.218\,m_0$	$1.57\,m_0$
In$_{0.53}$Ga$_{0.47}$As	$m_{x,crit}^*$	$0.041\,m_0$		
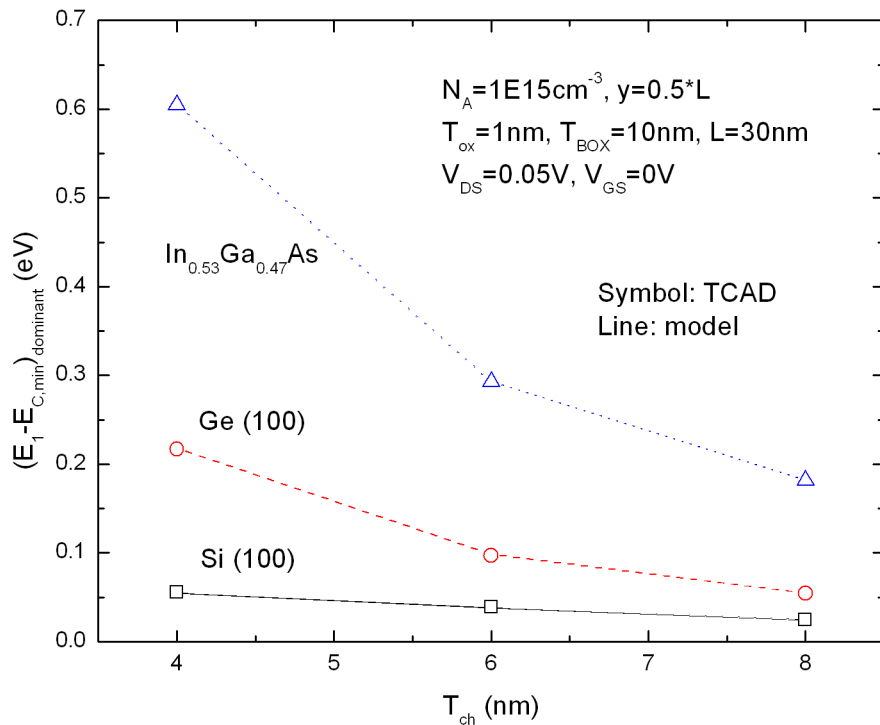
Fig. 3.8 The dominant $\left(E_1 - E_{C,\min}\right)$ for UTB devices with various channel materials.
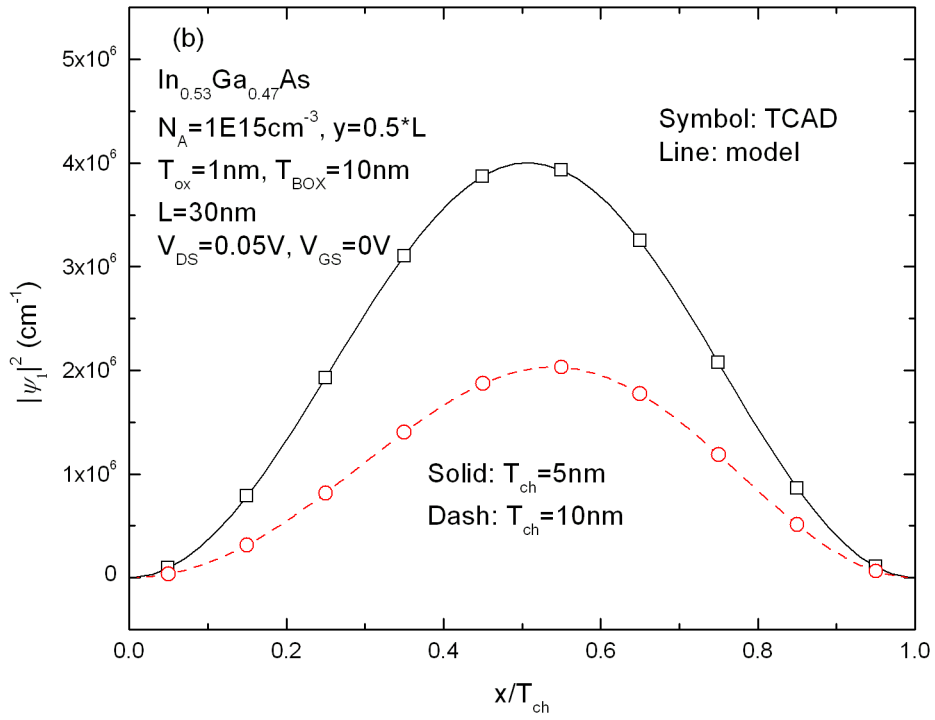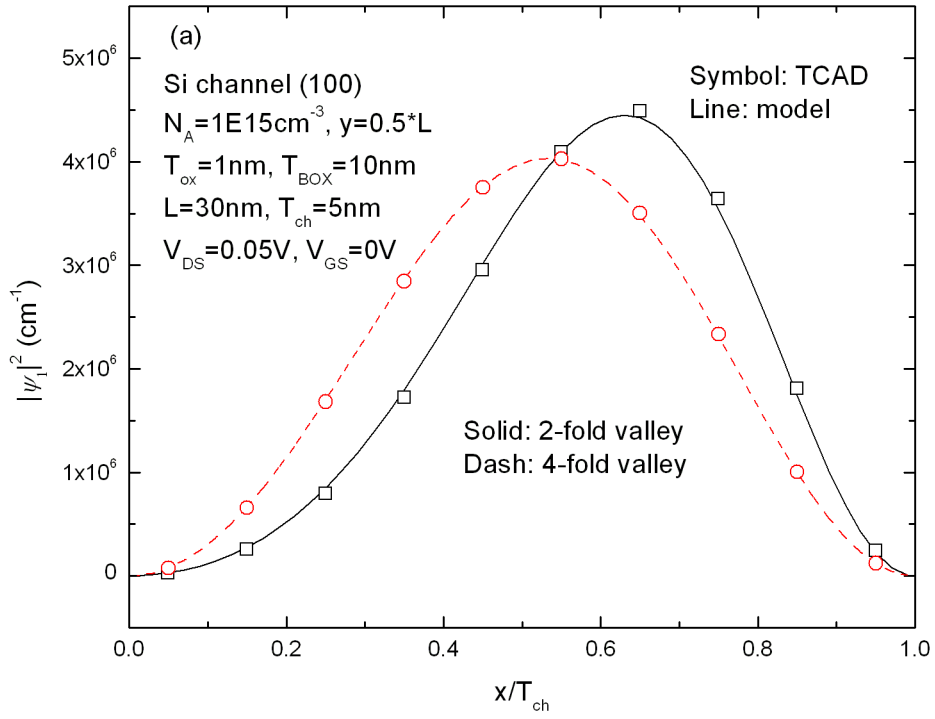
Fig. 3.9 The square of the first eigenfunction ($|\psi_1|^2$) for (a) Si-channel with (100) surface orientation and (b) In$_{0.53}$Ga$_{0.47}$As-channel UTB devices.
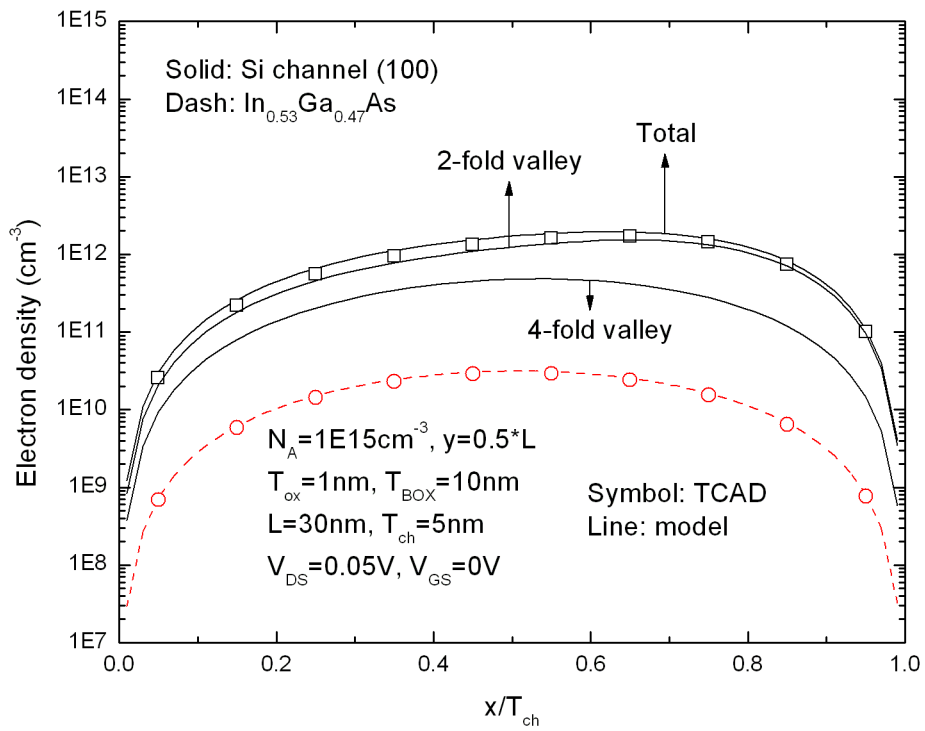
Fig. 3.10 The electron density of Si-channel with (100) surface orientation and In$_{0.53}$Ga$_{0.47}$As-channel UTB devices.

Chapter 4

Impact of Quantum-Mechanical Effects

on Threshold-Voltage Roll-Off

in UTB GeOI MOSFETs

4.1 Introduction

Germanium as a channel material has been proposed to enable mobility scaling. However, its higher permittivity makes it very susceptible to Short Channel Effects (SCEs). To improve the electrostatic integrity, ultra-thin-Body (UTB) Germanium-On-Insulator (GeOI) MOSFET has been proposed as a promising device architecture and shows better control of SCEs than the bulk counterpart [27]-[28]. By scaling down the channel thickness, UTB GeOI MOSFETs can show comparable subthreshold swing as compared with the UTB SOI counterparts [29]. As the channel thickness scales down, the quantum-mechanical effect becomes more significant and its impact on the threshold-voltage (V_T) roll-off in UTB SOI MOSFETs has been reported in [30]. However, the impact of quantum-mechanical effect on the V_T roll-off in UTB GeOI MOSFETs has rarely been examined.

In this chapter, we investigate the impact of quantum-mechanical effect on the V_T roll-off characteristics for UTB GeOI MOSFETs by the developed model in Chapter 3 and numerical solution of coupled Poisson and Schrödinger equations.

4.2 UTB GeOI Devices and Simulation

The schematic cross section of UTB structure was shown in Fig 2.1. In this study, the gate oxide thickness (T_{ox}) is 1nm, the channel thickness (T_{ch}) ranges from 4nm to 10nm, the channel length (L) ranges from 2.4 to 10 times the T_{ch} (proportional to T_{ch}), and the buried oxide thickness (T_{BOX}) ranges from 10nm to 20nm. The channel doping concentration (N_A) is $1 \times 10^{15} \text{cm}^{-3}$. Besides, we use the heavily-doped ($1 \times 10^{20} \text{cm}^{-3}$) silicon substrate and treat it as ground plane.

For UTB devices, our TCAD simulations self-consistently solves the Poisson's equation (for channel potential) and 1-D Schrödinger equation (for eigenenergy and eigenfunction) at each slice perpendicular to the interface between oxide and channel. The process of the numerical calculations doesn't have approximations. Therefore, the TCAD simulations can be exactly to assess quantum-mechanical effects for UTB GeOI devices.

In this study, the V_T is defined as the V_{GS} at which the average electron density of the cross-section at $y = y_{crit}$ exceeds the channel doping concentration. The y_{crit} stands for the position from the source of highest potential barrier for carrier flow. The y_{crit} is about $L/2$ for V_{DS}=0.05V, and about $L/3$ for V_{DS}=1V.

4.3 Results and Discussion

4.3.1 Channel Thickness

Fig. 4.1(a) and Fig 4.1(b) show the V_T roll-off of Ge- and Si-channel UTB devices with quantum-mechanical (QM) and classical (CL) considerations for T_{ch}=10nm and 5nm, respectively. In Fig 4.1(a), both the Ge- and Si-channel devices with QM consideration show larger V_T roll-off than that with the CL one. However, in Fig 4.1(b), the Si-channel UTB MOSFET with QM consideration shows comparable V_T roll-off as compared with that using the CL one. The Ge-channel UTB MOSFET with QM consideration even shows smaller V_T roll-off than that with the CL one.

In [30], Y. Omura reported that the V_T roll-off would be increased by QM effect in UTB SOI MOSFETs. Their study used the simulator with density-gradient model (DGM) [31]-[32]. In our study, we can see the same trend of increased V_T roll-off in UTB SOI MOSFET. However, the V_T roll-off is suppressed by QM effect for UTB GeOI MOSFET with T_{ch}=5nm.

Fig 4.1 can be explained by [33]-[34]

$$\Delta V_T^{QM} \cong m \cdot \Delta \phi^{QM} \tag{4.1}$$

, where m is the subthreshold slope factor, $\Delta \phi^{QM}$ is the surface potential shift, and ΔV_T^{QM} is the V_T shift due to QM effects. In this work, we choose the peak of the channel potential at $y = y_{crit}$ cross-section as the reference potential. Therefore, the $\left(E_1 - E_{C,\min}\right)$ at $y = y_{crit}$ can stand for the $q \cdot \Delta \phi^{QM}$ when considering QM effects.

Fig 4.2 shows the $\left(E_1 - E_{C,\min}\right)$ for GeOI devices with T_{ch}=10nm and 5nm. Fig 4.2(a) shows that for GeOI devices with T_{ch}=10nm, the $\left(E_1 - E_{C,\min}\right)$ of the long-channel ($L = 6T_{ch}$) GeOI device is about $2.5 \times \left(E_1 - E_{C,\min}\right)$ the short-channel

($L = 2.4T_{ch}$) one. In other words, the short-channel GeOI device with T_{ch}=10nm shows much smaller $\left(E_1 - E_{C,\min}\right)$ and thus smaller $\Delta\phi^{QM}$ as compared with the long-channel one. This leads to larger V_T roll-off observed in Fig 4.1(a). On the other hand, Fig 4.2(b) shows that for the T_{ch}=5nm GeOI devices, the $\Delta\phi^{QM}$ of the long-channel ($L = 6T_{ch}$) GeOI MOSFET is only $\sim 1.3 \times \left(E_1 - E_{C,\min}\right)$ the short-channel ($L = 2.4T_{ch}$) one. The m factor of the T_{ch}=5nm short-channel GeOI device, however, is about $2.5\times$ the long-channel one. Therefore, for the T_{ch}=5nm GeOI devices, the ΔV_T^{QM} of the short-channel device is larger than that of the long-channel one which results in the suppression of V_T roll-off observed in Fig 4.1(b).

4.3.2 Surface Orientation

Fig 4.3 shows the V_T roll-off of three surface orientations in UTB GeOI MOSFET for T_{ch}=4nm with QM and CL considerations. It can be seen that the V_T of the three orientations are (100)>(110)>(111). In Chapter 3, we have pointed out that the UTB GeOI device with T_{ch}=4nm has a critical effective mass ($m_{x,crit}^{*}$). From Table 3.2, we can find that the critical effective masses of (100), (110), and (111) are $0.117\,m_0$, $0.218\,m_0$, and $1.57\,m_0$, respectively. This means that the degree of QM effect is (100)>(110)>(111). It explains why the surface potential shifts ($\Delta\phi^{QM}$) shown in Fig 4.3(b) are (100)>(110>(111). In other word, the (100) orientation GeOI devices have the largest ΔV_T^{QM} and thus the largest V_T as shown in Fig 4.3(a).

Fig 4.3(b) also shows the ΔV_T^{SCE} of the three surface orientations. The ΔV_T^{SCE} can be expressed as

$$\Delta V_T^{SCE} = \left[\left(m \cdot \Delta\phi^{QM}\right)_{long} - \left(m \cdot \Delta\phi^{QM}\right)_{short}\right] + \left(V_{T,long} - V_{T,short}\right)^{CL} \tag{4.2}$$

Since the $\Delta\phi^{QM}$ shown in Fig 4.3(b) is almost the same for long- and short-channel GeOI devices, the equation (4.2) can be approximated as

$$\Delta V_T^{SCE} = \Delta\phi^{QM} \cdot \left(m_{long} - m_{short}\right) + \left(V_{T,long} - V_{T,short}\right)^{CL} \tag{4.3}$$

Because the (100) orientation GeOI devices possess the largest $\Delta\phi^{QM}$, they have the smallest ΔV_T^{SCE}. That is, the improvement of the V_T roll-off is the most significant for the (100) orientation GeOI devices. Note that $\left(m_{long} - m_{short}\right)$ is a negative number due to short channel effects (SCEs).

4.3.3 Drain Bias and Buried Oxide Thickness

Fig 4.4(a) illustrates the V_T roll-off of the GeOI devices at V_{DS} =1V. Its worse SCEs shows lower V_T and larger V_T roll-off than that with V_{DS} =0.05V. The ΔV_T^{QM} in the long-channel ($L = 6T_{ch}$ =30nm) GeOI devices are comparable between V_{DS} =1V and 0.05V as shown in Fig 4.4(a). Fig. 4.4(b) shows that for the short-channel ($L = 2.4T_{ch}$ =12nm) devices, high-drain-bias GeOI device shows larger improvement of roll-off (~0.3V) than the low-drain-bias one (~0.1V). This is because the high-drain-bias device shows both larger $\left(E_1 - E_{C,min}\right)$ (thus $\Delta\phi^{QM}$) and m factor than the low-drain-bias device as shown in Fig 4.5. For T_{ch} =5nm GeOI devices, the suppression of the V_T roll-off caused by the QM effect is more significant at high drain bias than at low drain bias.

41

Fig 4.6 shows the V_T roll-off of the T_{ch}=5nm GeOI devices with QM and CL considerations for T_{BOX}=20nm and 10nm. The long-channel ($L = 6T_{ch}$=30nm) device with T_{BOX}=20nm has comparable ΔV_T^{QM} as compared with the T_{BOX}=10nm device as shown in Fig 4.6(a). Fig 4.6(b) shows that at L=12nm, the GeOI device with T_{BOX}=20nm shows larger improvement of roll-off than that with T_{BOX}=10nm. This is because the T_{BOX}=20nm device shows both larger $\left(E_1 - E_{C,\min}\right)$ (thus $\Delta\phi^{QM}$) and m factor than the T_{BOX}=10nm device as shown in Fig 4.7. In other words, for the T_{ch}=5nm GeOI devices, the suppression of the V_T roll-off caused by the QM effect is more significant for T_{BOX}=20nm than for T_{BOX}=10nm. It should be noted that the GeOI device with T_{BOX}=20nm shows larger V_T roll-off with CL consideration due to the drain field penetration through the buried oxide, which may be compensated by the more significant suppression of the V_T roll-off due to QM effects. Therefore, when considering QM effect, the T_{ch}=5nm device with T_{BOX}=20nm shows comparable V_T roll-off as compared with the T_{BOX}=10nm device as shown in Fig 4.6.

In Fig 4.8, we show the difference between $\Delta V_T^{QM}{}_{long}$ and $\Delta V_T^{QM}{}_{short}$ for devices design with different buried oxide thicknesses and drain biases. The long-channel GeOI device is $L = 6T_{ch}$ and the short-channel one is $L = 2.4T_{ch}$. Then we make the intersections of the line $\left(\Delta V_T^{QM}{}_{long-channel} - \Delta V_T^{QM}{}_{short-channel}\right)$=0 and the curves in Fig 4.8 and define the T_{ch} locations of these intersections as the critical channel thicknesses ($T_{ch,crit}$). Therefore, for GeOI devices with $T_{ch}>T_{ch,crit}$, the V_T roll-off is enhanced by QM effect, while for GeOI devices with $T_{ch}<T_{ch,crit}$, the V_T roll-off is suppressed. Note that the GeOI devices with high drain bias and thick T_{BOX}

show larger $T_{ch,crit}$ than those with low drain bias and thin T_{BOX}.

4.4 Summary

We have investigated the impact of QM effects on the V_T roll-off in UTB GeOI MOSFETs. It shows two opposite trends for different ranges of T_{ch}. For GeOI devices with $T_{ch} > T_{ch,crit}$, the QM effect may increase the V_T roll-off. For GeOI devices with $T_{ch} < T_{ch,crit}$, the QM effect is found to suppress the V_T roll-off. We also find that the value of $T_{ch,crit}$ increases with drain bias and T_{BOX}. This quantum-mechanical impact on short channel V_T roll-off should be considered when designing/evaluating UTB GeOI devices.
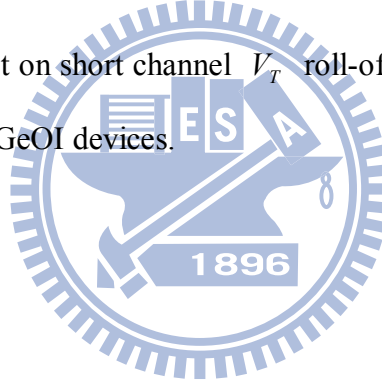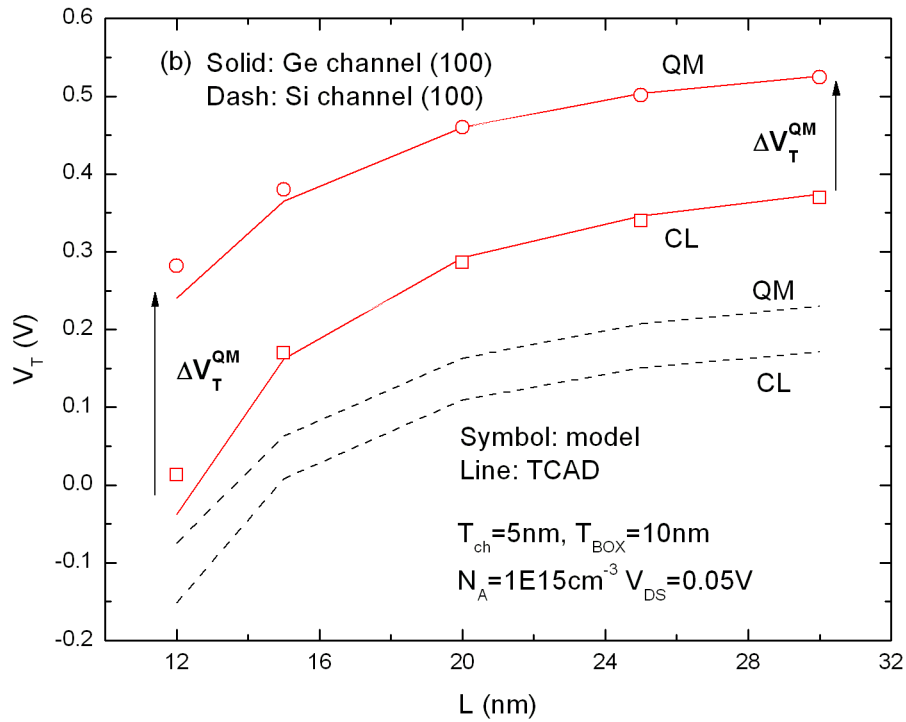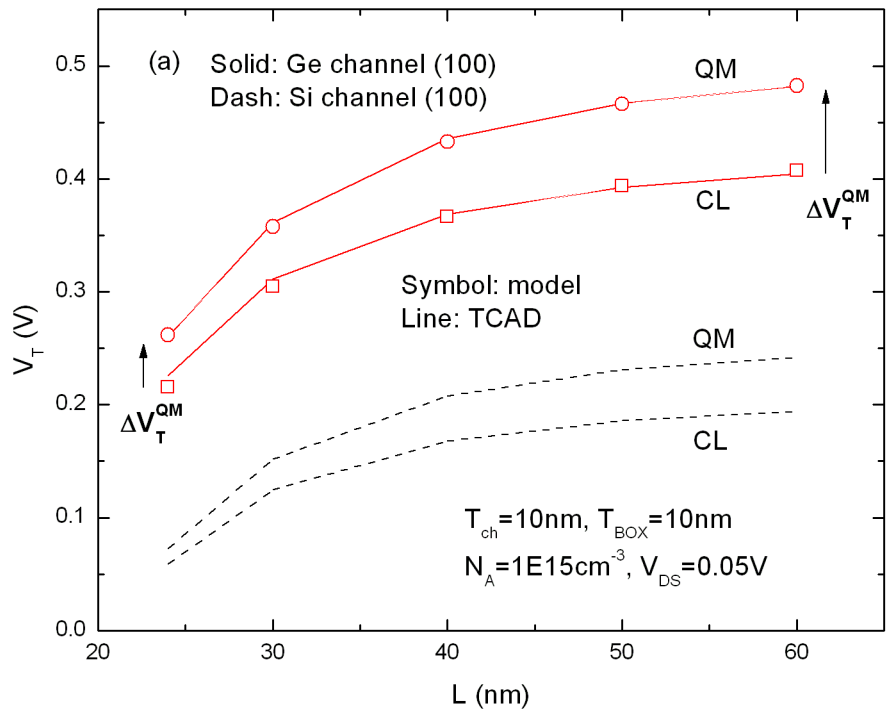
Fig. 4.1 The V_T roll-off of Ge- and Si-channel UTB devices with (a) T_{ch}=10nm and (b) T_{ch}=5nm.
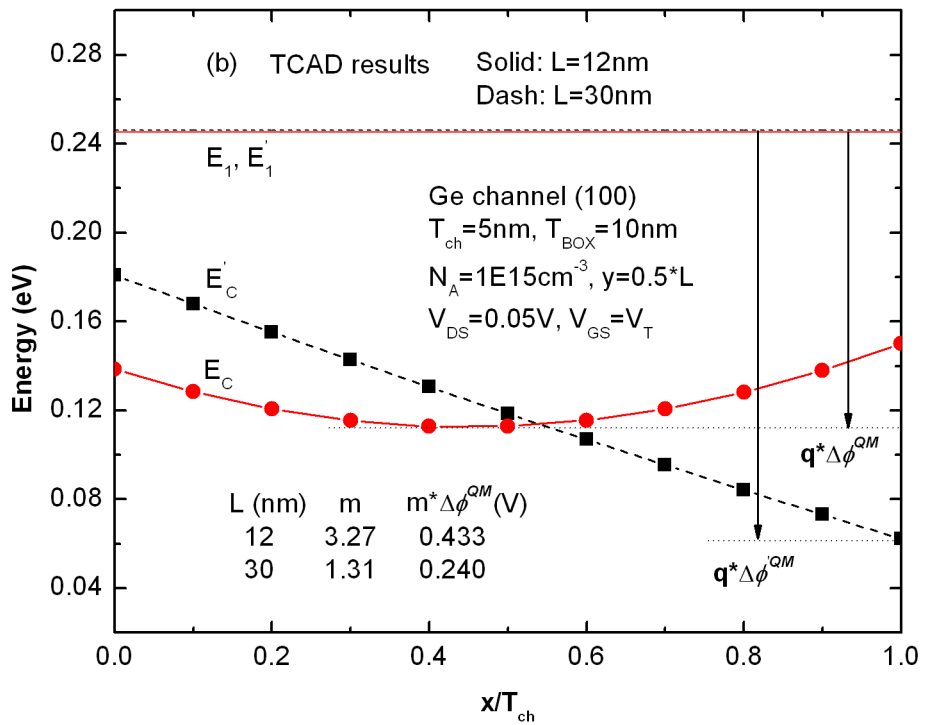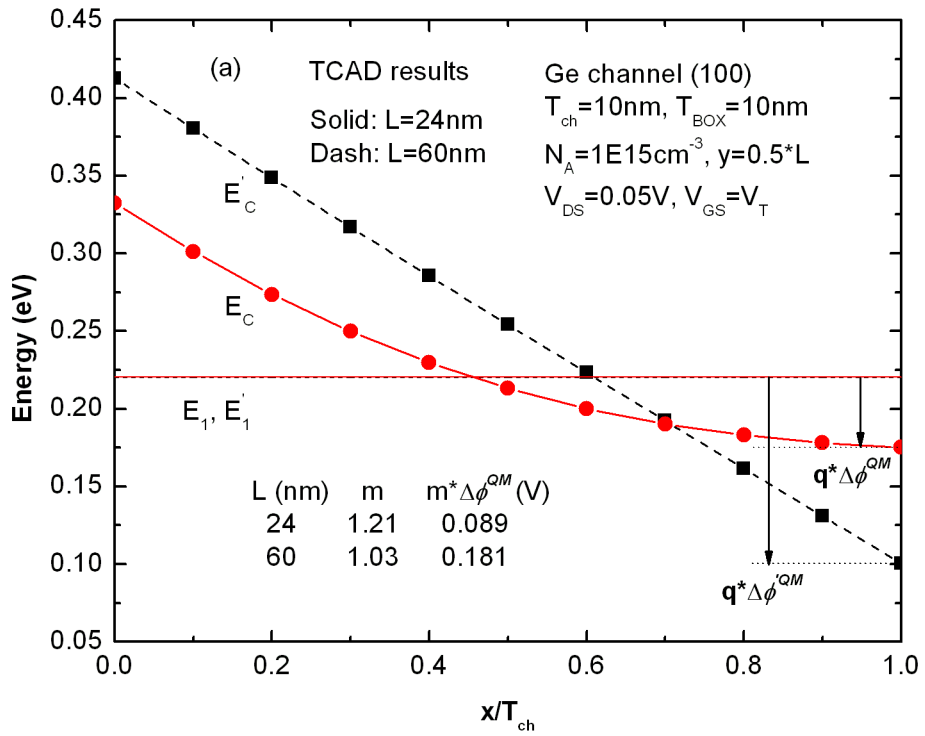
Fig. 4.2 $\left(E_1 - E_{C,\min}\right)$ and $m \cdot \Delta\phi^{QM}$ comparisons between short- and long-channel devices with (a) T_{ch}=10nm and (b) T_{ch}=5nm.
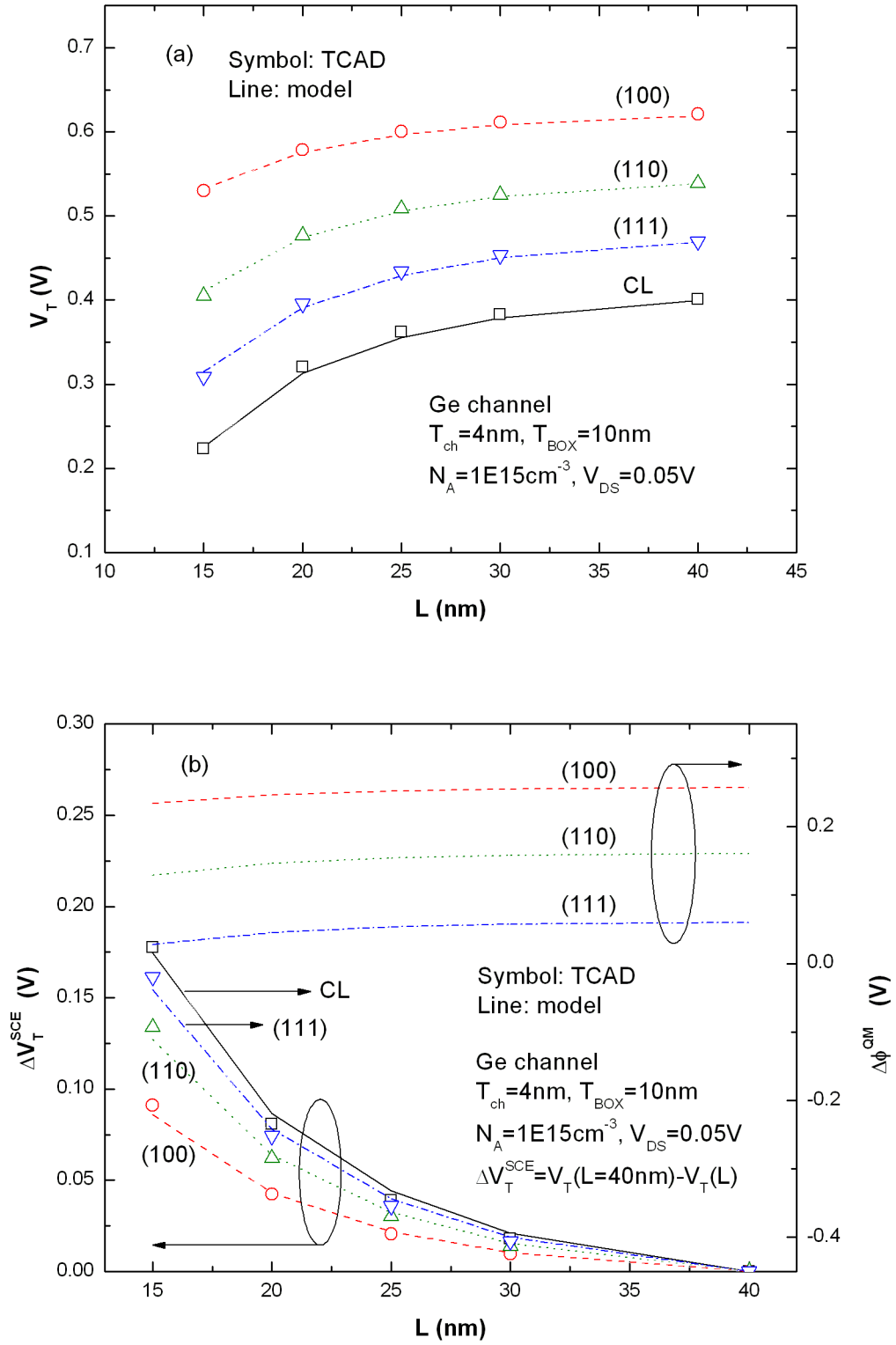
Fig. 4.3 (a) The V_T, (b) the V_T roll-off (ΔV_T^{SCE}), and the $\Delta\phi^{QM}$ of (100), (110), and (111) surface orientations for T_{ch}=4nm GeOI devices..
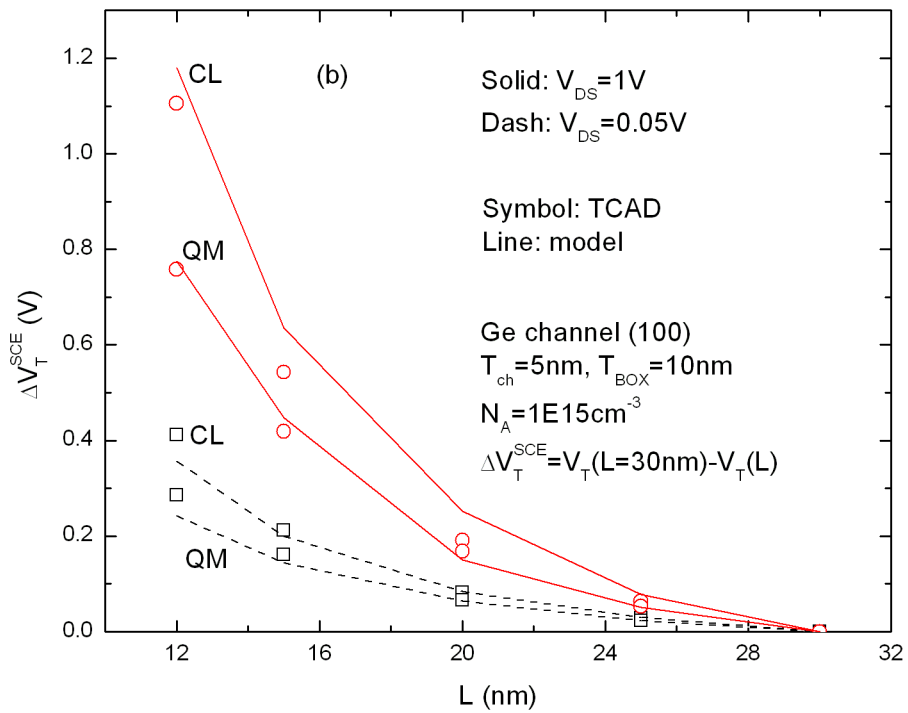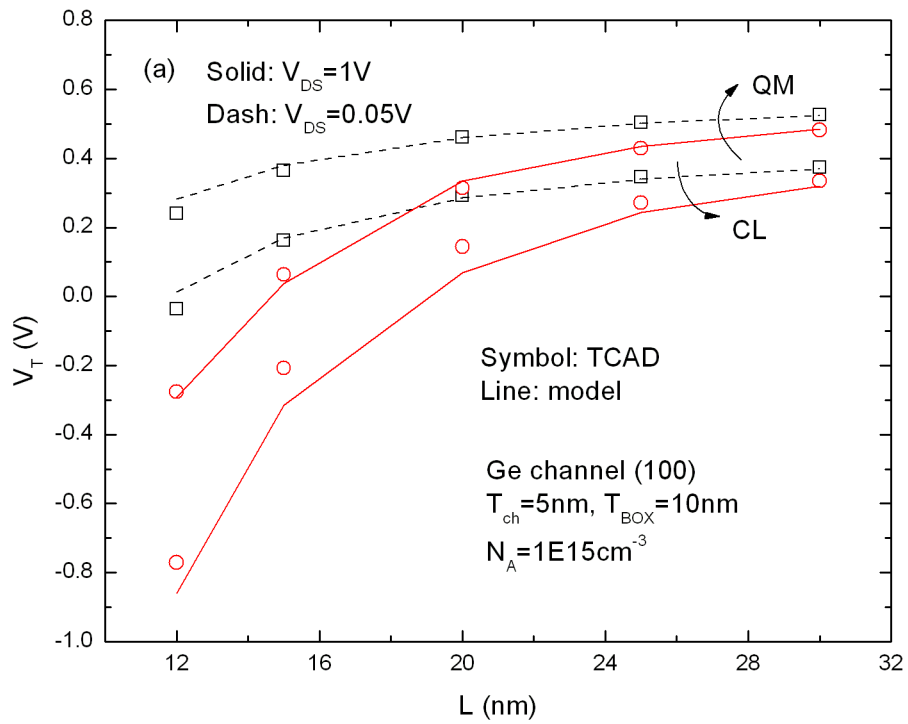
Fig. 4.4 (a) The V_T and (b) The V_T roll-off of the T_{ch}=5nm GeOI devices

at V_{DS}=0.05V and 1V.
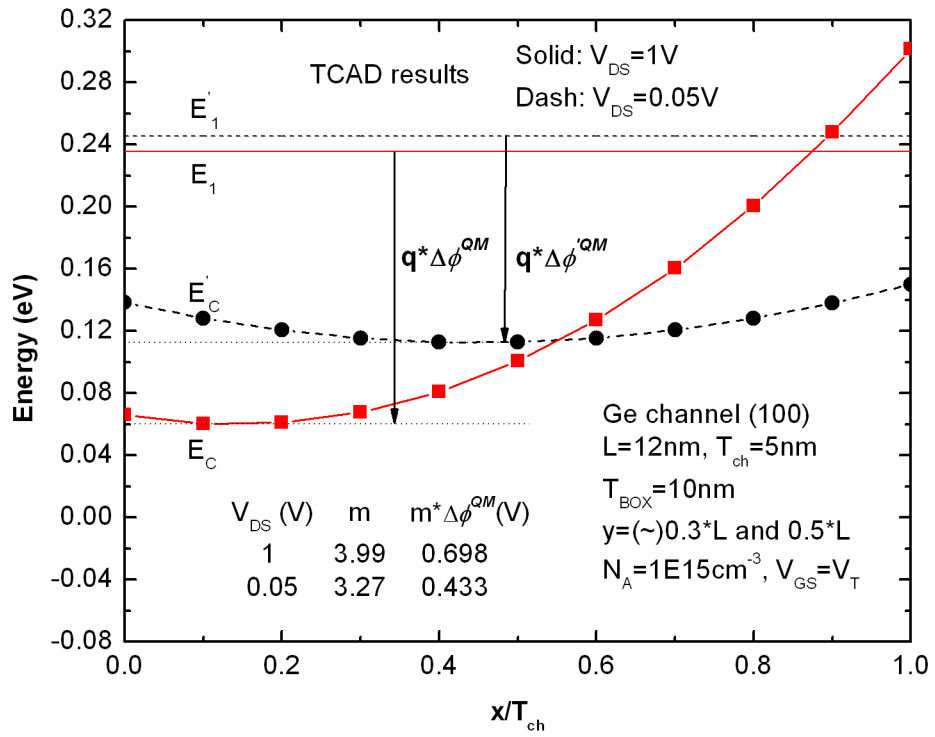
Fig. 4.5 The GeOI device (T_{ch}=5nm, L=12nm) with V_{DS}=1V shows larger m and $m \cdot \Delta\phi^{QM}$ than that with V_{DS}=0.05V.

.
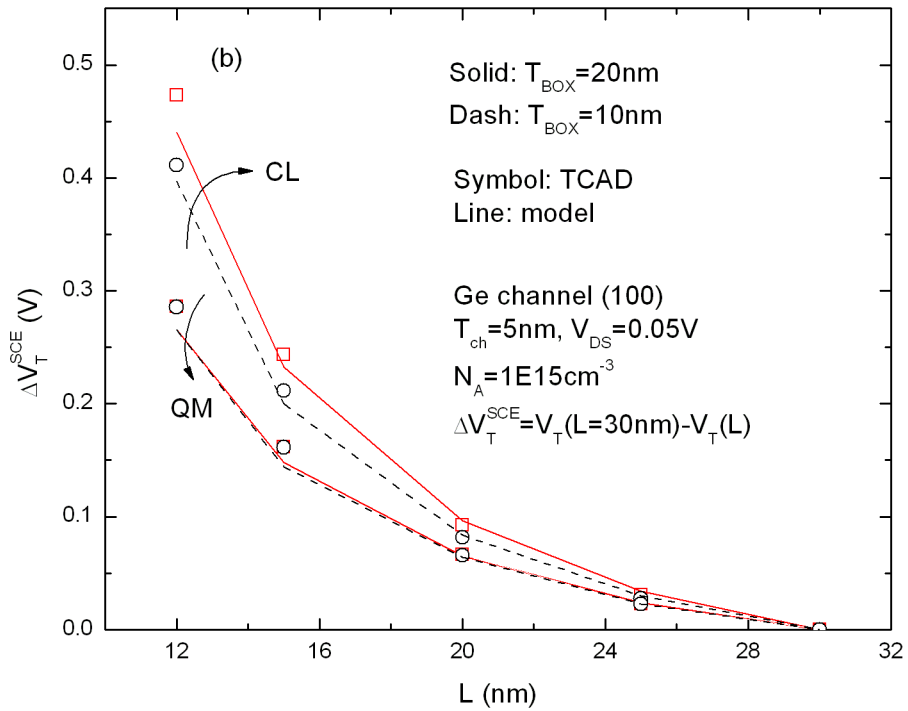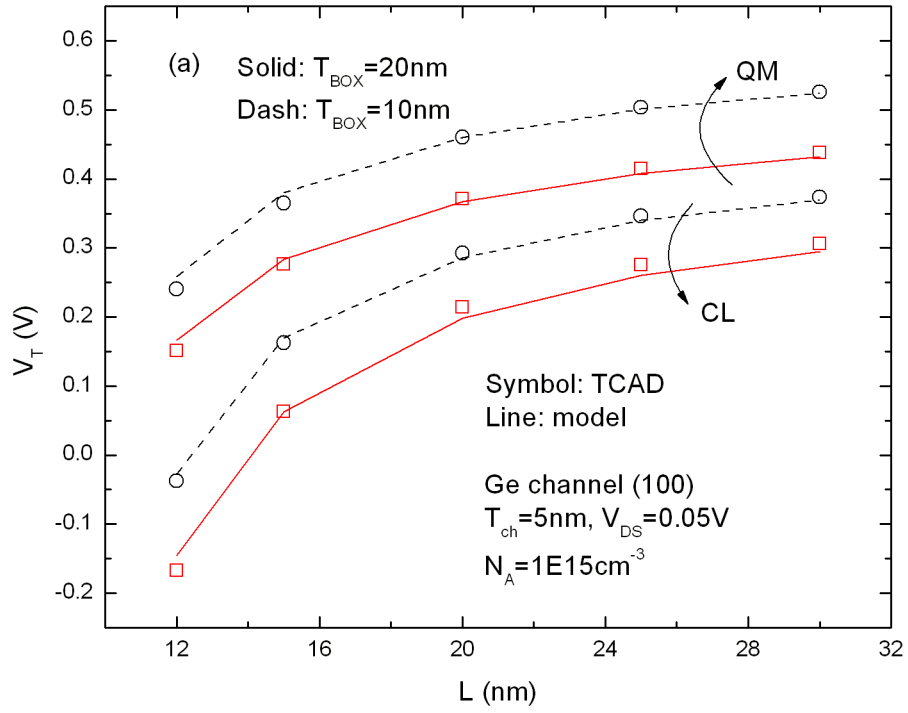
Fig. 4.6 (a) The V_T and (b) The V_T roll-off of the T_{ch}=5nm GeOI devices with T_{BOX}=20nm and 10nm.
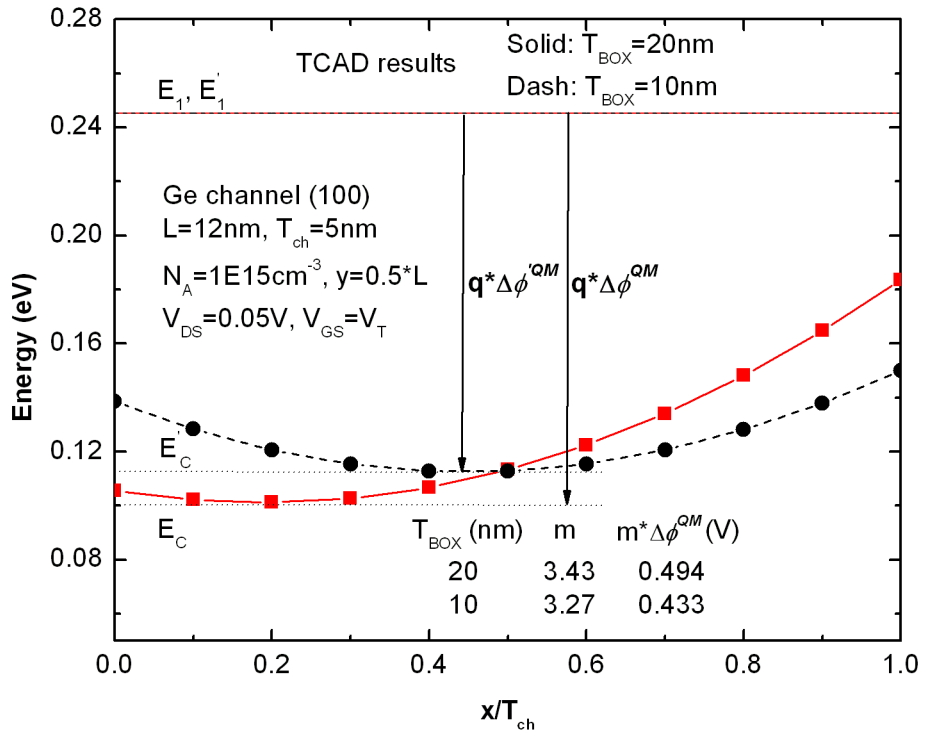
Fig. 4.7 The GeOI device (T_{ch} =5nm, L =12nm) with T_{BOX} =20nm shows larger m and $m \cdot \Delta \phi^{QM}$ than that with T_{BOX} =10nm.

.
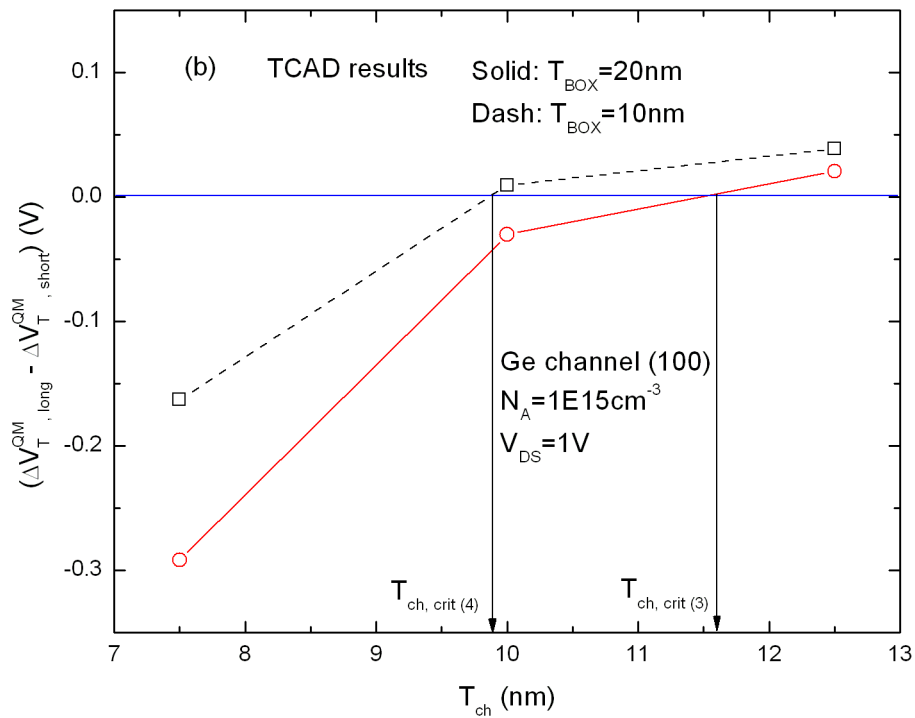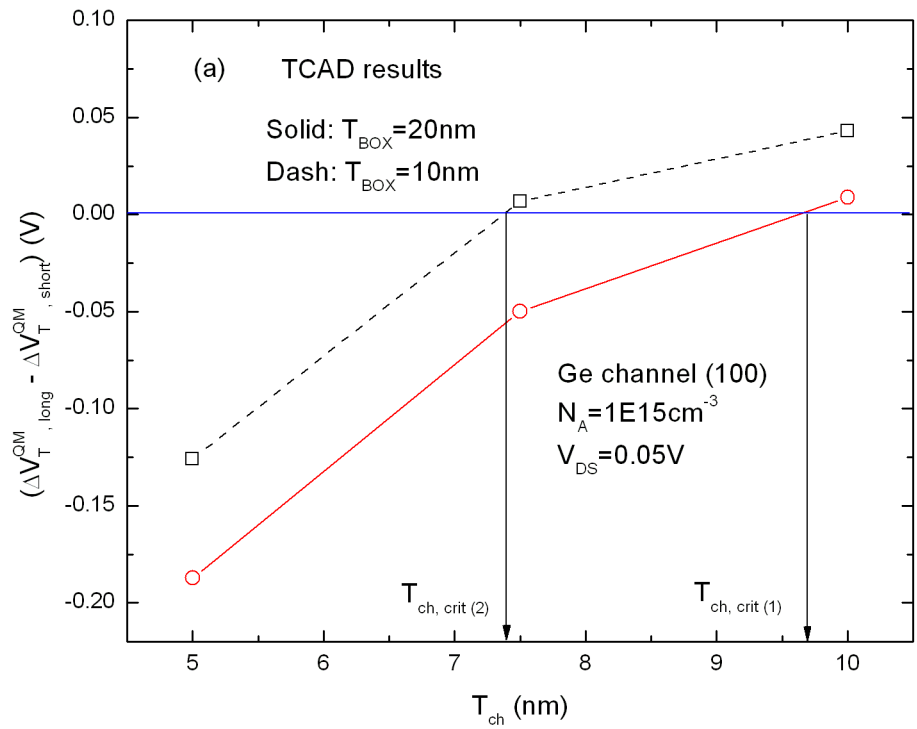
Fig 4.8 The ($\Delta V_T^{QM}{}_{long-channel} - \Delta V_T^{QM}{}_{short-channel}$) for T_{BOX} =20nm and 10nm GeOI

devices at (a) V_{DS} =0.05V and (b) V_{DS} =1V.

Chapter 5
Conclusions

We have theoretically investigated the impact of quantum-confinement effects on V_T roll-off for UTB GeOI MOSFETs with thin BOX under subthreshold region. To determine V_T of UTB devices, we derived a quantum-confinement model base on a parabolic form of channel potential. This parabolic channel potential is simplified from the series solution of Poisson's equation and has the correct dependence of channel length. Therefore, this quantum-confinement model can accurately reveal the subthreshold characteristics of UTB devices when considering short channel effects (SCEs) such as V_T roll-off.

By using the quantum-confinement model and TCAD simulations which self-consistently solve the Poisson's equation and Schrödinger equation, we find that in UTB GeOI MOSFETs, there exists two trends of V_T roll-off for different ranges of T_{ch}, either increased or suppressed V_T roll-off caused by quantum confinement. The critical channel thickness ($T_{ch,crit}$) represents the crossover point between the two trends. For GeOI devices with $T_{ch} > T_{ch,crit}$, the QM effect increases the V_T roll-off. On the other hand, the QM effect is found to suppress the V_T roll-off when $T_{ch} < T_{ch,crit}$. The value of $T_{ch,crit}$ increases with the drain bias and T_{BOX}. For a given T_{BOX}, the $T_{ch,crit}$ for Ge-channel devices is larger than that for Si-channel ones. The impact of quantum-confinement on the V_T roll-off must be considered when one-to-one comparisons between UTB GeOI and SOI MOSFETs.

References

[1] C. O. Chui, H. Kim, D. Chi, B. B. Triplett, P. C. Melntyre, and K. C. Saraswat, "A sub-400℃ germanium MOSFET technology with high-k dielectric and metal gate," in *IEDM Tech. Dig.*, 2002, pp. 437-440.

[2] H. Shang, K. L. Lee, P. Kozlowski, C. D'Emic, I. Babich, E. Sikorski, M. Ieong, H.-S. P. Wong, K. Guarini, and W. Haensch, "Self-aligned n-channel germanium MOSFETs with a thin Ge oxynitride gate dielectric and tungsten gate," *IEEE Electron Device Lett.*, vol. 25, no. 3, pp. 135-137, March 2004.

[3] C. O. Chui, F. Ito, and K. C. Saraswat, "Nanoscale germanium MOS dielectrics – Part I: germanium oxynitrides," *IEEE Trans. on Electron Device*, vol. 53, no. 7, pp. 1501-1508, July 2006.

[4] E. Pop, C. O. Chui, S. Sinha, R. Dutton, and K. Goodson, "Electro-thermal comparison and performance optimization of Thin-Body SOI and GOI MOSFETs," in *IEDM Tech. Dig.*, 2004, pp. 411-414.

[5] S. W. Bedell, A. Majumdar, J. A. Ott, J. Arnold, K. Fogel, S. J. Koester, and D. K. Sadana, "Mobility scaling in short-channel length strained Ge-on-Insulator P-MOSFETs," *IEEE Electron Device Lett.*, vol. 29, no. 7, pp. 811-813, July 2008.

[6] V. Hu, Y. S. Wu, and P. Su, "Investigation of electrostatic integrity for ultra-thin-body GeOI MOSFET using analytical solution of Poisson's equation," *Semicond. Sci. Technol.*, vol. 24, no. 4, April 2009.

[7] Y. S. Wu and P. Su, "Analytical quantum-confinement model for short-channel gate-all-around MOSFETs under subthreshol region," *IEEE Trans. on Electron Device*, vol. 56, no. 11, November 2009.

[8] V. P. Trivede and J. G. Fossum, "Quantum-mechanical effects on the threshold

voltage of undoped double-gate MOSFETs," *IEEE Electron Device Lett.*, vol. 26, no. 8, pp. 579-582, August 2005.

[9] H. K. Lim and J. G. Fossum, "Threshold voltage of thin-film silicon-on-insulator (SOI) MOSFETs," *IEEE Trans. on Electron Device*, vol. ED-30, no. 10, pp. 1244-1251, Oct. 1983.

[10] S. Monfray, M. P. Samson, D. Dutartre, T. Ernst, E. Rouchouze, D. Renaud, B. Guillaumot, D. Chanemougame, G. Rabille, S. Borel, J. P. Colona, C. Arvet, N. Loubet, Y. Campidelli, J. M. Hartmann, L. Vandroux, D. Bensahel, A. Toffoli, F. Allain, A. Margin, L. Clement, A. Quiroga, S. Deleonibus, and T. Skotnicki, "Localized SOI technology: An innovative low cost self aligned process for ultra thin Si-film on thin BOX integration for low power applications," in *IEDM Tech. Dig.*, 2007, pp. 693-696.

[11] T. Ohtou, N. Sugii, and T. Hiramoto, "Impact of parameter variations and random dopant fluctuations on short channel fully depleted SOI MOSFETs with extremely thin BOX," *IEEE Electron Device Lett.*, vol. 28, no. 8, pp. 740-742, Aug. 2007.

[12] Y. Morita, R. Tsuchiya, T. Ishigaki, N. Sugii, T. Iwamatsu, T. Ipposhi, H. Oda, Y. Inoue, K. Torii, and S. Kimura, "Smallest Vth variability achieved by intrinsic silicon on thin BOX (SOTB) CMOS with single metal gate," in *VLSI Symp. Tech. Dig.*, 2008, pp. 166-167.

[13] V. Hu, Y. S. Wu, M. L. Fan, P. Su, and C. T. Chuang, "Static noise margin of ultrathin-body SOI subthreshold SRAM cells – An assessment based on analytical solutions of Poisson's equation," *IEEE Trans. on Electron Device*, vol. 56, no. 9, pp. 2120-2127, September 2009.

[14] V. Hu, Y. S. Wu, and P. Su, "Investigation of electrostatic integrity for ultra-thin-body Germanium-On-Nothing (GeON) MOSFET," *IEEE Trans. on*

Nanotechnology, November 2010 (accepted).

[15] V. Hu, Y. S. Wu, and P. Su, "Investigation of electrostatic integrity for ultra-thin-body GeOI MOSFET using analytical solution of Poisson's equation," *Semicond. Sci. Technol.*, vol. 24, no. 4, April 2009.

[16] Y. Taur and T. H. Ning, "Fundamentals of Modern VLSI Devices," pp. 117, Cambridge University Press, 1998.

[17] Y. Omura, S. Horiguchi, M. tabe, and K. Kishi, "Quantum-mechanical effects on the threshold voltage of ultrathin-SOI nMOSFETs," *IEEE Trans. on Electron Device*, vol. 14, no. 12, pp. 569-571, December 1993

[18] M. J. Gilbert and D. K. Ferry, "Efficient quantum three-dimensional modeling of fully depleted ballistic silicon-on-insulator metal-oxide-semiconductor field-effect-transistors," *J. App. Phys.*, vol. 95, no. 12, June 2004.

[19] S. I. Takagi, J. L. Jeffrey, J. Welser, and J. F. Gibbons, " Comparative study of phonon-limited mobility of two-dimensional electrons in strained and unstrained Si metal-oxide-semiconductor field-effect transistors," *J. App. Phys.*, vol. 80, no. 3, August 1996.

[20] Y. Liu, N. Neophytou, G. Klimeck, and M. S. Lundstrom, "Band-structure effects on the performance of III-V ultrathin-body SOI MOSFETs," *IEEE Trans. on Electron Device*, vol. 55, no. 5., May 2008.

[21] Y. S. Wu, M. L. Fan, and P. Su, "Impact of surface orientation on Vth variability of FinFET," *Silicon Nanoelectronics Workshop*, June 2010.

[22] Y. S. Wu and P. Su, "Analytical quantum-confinement model for short-channel gate-all-around MOSFETs under subthreshol region," *IEEE Trans. on Electron Device*, vol. 56, no. 11, November 2009.

[23] B. G. Streetman and S. K. Banerjee, "Solid state electronic devices," Appendix IV, pp. 523-527, Pearson Prentice Hall, sixth edition.

[24] F. Stern and W. E. Howard, "Properties of semiconductor surface inversion layers in the electric quantum limit," *Phys. Review*, vol. 163, no. 3, 1967.

[25] K. H. Goetz, D. Bimberg, H. Jurgensen, J. Selders, A.V. Solomonov, G. F. Glinskii, and M. Razeghi, "Optical and crystallographic properties and impurity incorporation of $Ga_xIn_{1-x}As$ (0.44<x<0.49) grown by liquid phase epitaxy, vapor phase epitaxy, and metal organic chemical vapor deposition," *J. Appl. Phys.*, vol. 54, no.8, pp. 4543-4552, 1983.

[26] T. P. Pearsall, "*GaInAsP Alloy Semiconductors*," John Wiley and Sons., 1982.

[27] E. Pop, C. O. Chui, S. Sinha, R. Dutton, and K. Goodson, "Electron-thermal comparison and performance optimization of thin-body SOI and GOI MOSFETs," in *IEDM Tech. Dig.*, 2004, pp. 411-414.

[28] S. W. Bedell, A. Majumdar, J. A. Ott, J. Arnold, K. Fogel, S. J. Koester, and D. K. Sadana, "Mobility scaling in short-channel length strained Ge-on-Insulator P-MOSFETs," *IEEE Electron Device Lett.*, vol. 29, no. 7, pp. 811-813, July 2008.

[29] V. Hu, Y. S. Wu, and P. Su, "Investigation of Electrostatic Integrity for Ultra-Thin-Body GeOI MOSFET Using Analytical Solution of Poisson's Equation," *Semicond. Sci. Technol.*, vol. 24, no. 4, April 2009.

[30] Y. Omura, H. Konishi, and S. Sato, "Quantum-mechanical suppression and enhancement of SCEs in ultrathin SOI MOSFETs," *IEEE Trans. on Electron Device*, vol. 53, no. 4, pp. 677-684, April 2006.

[31] M. G. Ancona and H. F. Tiersten, "Macroscopic physics of the silicon inversion layer," *Phys. Rev. B, Condens. Matter*, vol. 35, no. 15, pp. 7959-7965, May 1987.

[32] M. G. Ancona and G. J. Iafrate, "Quantum correction to the equation of state of an electron gas in a semiconductor," *Phys. Rev. B, Condens. Matter*, vol. 39, no. 13, pp. 9536-9540, May 1989.

[33] Y. Taur and T. H. Ning, "Fundamentals of Modern VLSI Devices," pp. 198, Cambridge University Press, 1998.

[34] V. P. Trivede and J. G. Fossum, "Quantum-mechanical effects on the threshold voltage of undoped double-gate MOSFETs," *IEEE Electron Device Lett.*, vol. 26, no. 8, pp. 579-582, August 2005.
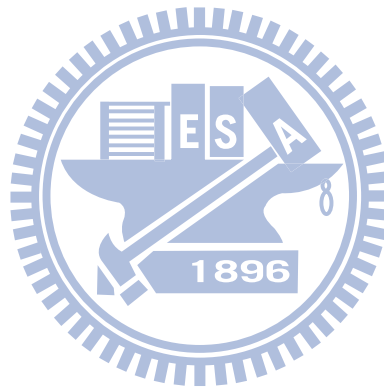
簡　歷

姓名：謝欣原

生日：74 年 8 月 19 日

出生地：台灣省雲林縣

地址：高雄縣鳳山市誠義路 185 巷 1 號

學歷：

　　高雄市立高雄高級中學畢　　　　　　（89 年 9 月~92 年 6 月）

　　國立交通大學電子工程學系畢　　　　（93 年 9 月~97 年 6 月）

　　國立交通大學電子研究所碩士班畢　　（97 年 9 月~99 年 8 月）

碩士論文題目：

超薄絕緣鍺金氧半場效電晶體在量子侷限下的

短通道效應模型與分析

Modeling and Investigation of Short-Channel Effects for

Ultra-Thin-Body Germanium-On-Insulator MOSFETs

Considering Quantum Confinement